Dopamine differentially modulates the size of projection neuron ensembles in the intact and dopamine-depleted striatum

Marta Maltese, Jeffrey R. March, Alexander G. Bashaw, Nicolas X. Tritsch[#]

Neuroscience Institute, New York University School of Medicine, New York, NY 10016, U.S.A., and Fresco Institute for Parkinson's and Movement Disorders, New York University Langone Health, New York, NY 10016, U.S.A.

[#] correspondence and requests for materials should be addressed to N.X.T. (email: nicolas.tritsch@nyulangone.org)

ABSTRACT

Dopamine (DA) is a critical modulator of brain circuits that control voluntary movements, but our understanding of its influence on the activity of target neurons *in vivo* remains limited. Here, we use two-photon Ca^{2+} imaging to monitor the activity of direct and indirect-pathway spiny projection neurons (SPNs) simultaneously in the striatum of behaving mice during acute and prolonged manipulations of DA signaling. We find that increasing and decreasing DA biases striatal activity towards the direct and indirect pathways, respectively, by changing the overall number of SPNs recruited during behavior in a manner not predicted by existing models of DA function. This modulation is drastically altered in a model of Parkinson's disease. Our results reveal a previously unappreciated population-level influence of DA on striatal output and provide novel insights into the pathophysiology of Parkinson's disease.

INTRODUCTION

The neuromodulator dopamine (DA) is an essential component of basal ganglia circuits that control goal-directed behaviors. Considerable evidence in humans, primates and rodents implicates DA in supporting motor learning and in executing vigorous movements via its actions in the striatum, the principal input nucleus to the basal ganglia (Graybiel 2005; Turner & Desmurget 2010; Dudman & Krakauer 2016; Klaus et al., 2019). The striatum mainly consists of two large populations of inhibitory spiny projection neurons (SPNs) that belong to the direct and indirect pathways (dSPNs and iSPNs, respectively). The former directly inhibits output nuclei of the basal ganglia, including the internal globus pallidus and substantia nigra pars reticulata, while the latter promotes their activity indirectly by way of the external globus pallidus and subthalamic nucleus. Although long believed to exert opposite effects on movement, dSPNs and iSPNs are now known to be concurrently active and to work in concert to produce coherent sequences of voluntary movements (Cui et al., 2013; Barbera et al., 2016; Klaus et al., 2017; Markowitz et al., 2018; Meng et al., 2018; Parker et al., 2018; Sheng et al., 2019). How DA influences the activity of dSPNs and iSPNs *in vivo* to affect movement, however, remains poorly understood.

Because dSPNs express $G\alpha_s$-coupled D_1-type DA receptors and iSPNs $G\alpha_i$-coupled D_2-type DA receptors, DA is widely believed to differentially modulate both pathways and to promote imbalances that impact how the basal ganglia contribute to behavior (Gerfen & Surmeier 2011; Nelson & Kreitzer 2014; Klaus et al., 2019). Electrophysiological studies in brain slices have identified several ion channels and synaptic properties in SPNs susceptible to differential modulation by DA on both short and long timescales (Tritsch & Sabatini 2012; Zhai et al., 2019). DA has for instance been shown to modify the intrinsic excitability of SPNs over the course of seconds to minutes, increasing and reducing the number of action potentials produced by dSPNs and iSPNs in response to somatic current injection, respectively (Hernandez-Lopez et al., 2000; Ericsson et al., 2013; Planert et al., 2013; Lahiri & Bevan 2020). These effects may account for DA's ability to transiently motivate behavior and invigorate motor actions (Panigrahi et al., 2015; Hamid et al., 2016; da Silva et al., 2018). DA receptor signaling also promotes the long-term potentiation and depression of cortico-striatal glutamatergic synapses in dSPNs and iSPNs (Calabresi et al., 2007; Pawlak & Kerr 2008; Shen et al., 2008). Such plasticity may underlie motor learning and the formation of motor habits by striatal circuits (Koralek et al., 2012; Yttri & Dudman 2016; Iino et al., 2020).

Although *ex vivo* studies provide compelling evidence that DA directly promotes the activation of dSPNs and impedes that of iSPNs, there are good reasons to believe that DA's modulatory effects *in vivo* may be more complex. First, DA does not act exclusively onto SPNs. DA receptors are also found on excitatory afferents, inhibitory SPN collaterals and striatal

interneurons, all of which participate in shaping striatal output (Tritsch & Sabatini 2012; Zhai et al., 2019). Second, SPNs are constantly exposed to DA, as midbrain DA neurons fire action potentials tonically at 3-10 Hz (Grace & Bunney 1984; Cohen et al., 2012). Given that a single pulse of DA alters the excitability of SPNs for several minutes (Lahiri & Bevan 2020), additional modulation by rising DA may be occluded *in vivo*. Alternatively, the relatively low affinity of D_1 receptors for DA compared to D_2 receptors raises the possibility that dSPNs may only be sensitive to rising DA levels, while iSPNs may selectively respond to drops in extracellular DA (Beaulieu & Gainetdinov 2011; Iino et al., 2020; Lee et al., 2020). Third, although *in vivo* studies comparing SPN discharge before and after DA neuron lesions in animal models of Parkinson's disease support the view that DA differentially modulates firing rates in dSPNs and iSPNs (Mallet et al., 2006; Ryan et al., 2018), they do not directly speak to DA's actions under physiological conditions, as chronic loss of DA evokes widespread homeostatic adaptations in striatal circuits (Zhai et al., 2019). Lastly, whether DA modulates other aspects of striatal output in addition to discharge rates, such as bursting or population-level striatal activity patterns, has been explored less extensively.

Recent imaging studies show that distinct motor actions are represented in striatum by separate groups – or ensembles – of SPNs, and that individual renditions of a given action recruit a sparse subset of SPNs from these larger action-specific ensembles (Barbera et al., 2016; Klaus et al., 2017; Markowitz et al., 2018). It is presently not clear how plastic these neural representations are, and if DA plays a role in sculpting them. Here, we test this possibility using two-photon Ca^{2+} imaging to monitor dSPN and iSPN ensembles simultaneously in the striatum of behaving mice. We report that acute and chronic DA manipulations strongly modify the overall size of movement-related ensembles in both dSPNs and iSPNs, resulting in pathway imbalances. Importantly, DA receptor signaling does not modulate dSPN and iSPN ensembles in opposite ways. Whereas the size of iSPN ensembles is inversely related to DA signaling, dSPN ensembles follow an 'inverted-U' shaped response. Chronic loss of midbrain DA neurons in a model of advanced Parkinson's disease is associated with a selective decrease in the number of active dSPNs and with dramatic changes in how movement-related dSPN ensembles respond to DA. Our results therefore reveal that, in addition to its effects on firing rates, DA regulates striatal output by reconfiguring its movement-related ensemble code.

RESULTS

Simultaneous imaging of dSPN and iSPN activity

To resolve the activity of individual striatal neurons *in vivo*, we expressed the Ca^{2+} indicator GCaMP6f (Chen et al., 2013) virally in the dorsolateral striatum under control of the synapsin promoter to label all neurons (**Figure 1A**). Most experiments were conducted using *Drd1a*^{tdTomato}

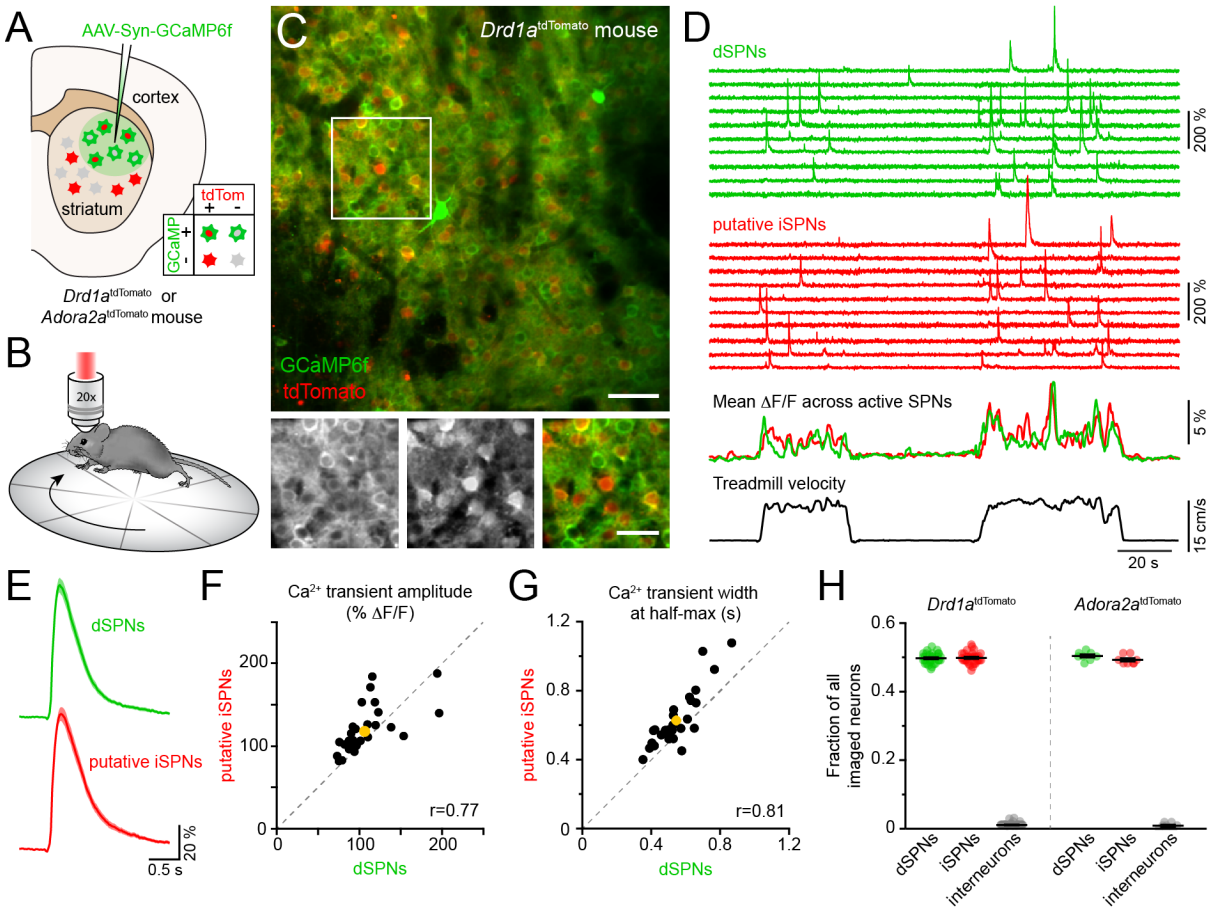

Figure 1. Simultaneous Ca^{2+} imaging from dSPNs and iSPNs

A,B. Experimental setup. GCaMP6f was virally expressed in dorsolateral striatum neurons (**A**) in mice expressing tdTomato in dSPNs (*Drd1a*^{tdTomato}) or iSPNs (*Adora2a*^{tdTomato}), and imaged by two-photon microscopy through an implanted imaging window while mice locomote on a circular treadmill (**B**).

C. *Top*: representative two-photon maximum projection image of dorsolateral striatum in a *Drd1a*^{tdTomato} mouse. Red: dSPNs, green: striatal neurons virally transduced to express GCaMP6f (scale bar: 50 μm). *Inset* shown at *bottom* in green (*left*) and red (*middle*) channels only, and composite (*right*; scale bar: 30 μm).

D. *Top*: example Ca^{2+} fluorescence traces from dSPNs (green) and putative iSPNs (red) in a *Drd1a*^{tdTomato} mouse. *Middle*: Mean ΔF/F across all active dSPNs and iSPNs. *Bottom*: treadmill velocity highlighting two self-initiated locomotor bouts.

E. Mean Ca^{2+} transient waveform (± s.e.m) imaged from active dSPNs and putative iSPNs in *Drd1a*^{tdTomato} mice.

F. Comparison of Ca^{2+} transient amplitude in dSPNs versus putative iSPNs in *Drd1a*^{tdTomato} mice (n = 30 FOVs from 18 mice). Mean ± s.e.m is depicted in yellow, and unity as dashed gray line. *r*: Spearman correlation coefficient.

G. Same as **f** for Ca^{2+} transient width at half-max in dSPNs versus iSPNs.

H. Fraction of all imaged neurons assigned to dSPNs, iSPNs and interneurons in *Drd1a*^{tdTomato} (n = 30 FOVs from 18 mice) and *Adora2a*^{tdTomato} (n = 8 FOVs in 4 mice) mice.

transgenic mice (N = 18), in which dSPNs are selectively labeled red (Ade et al., 2011). We subsequently performed two-photon microscopy through an imaging window chronically implanted in cortex over dorsal striatum (Howe & Dombeck 2016; Bloem et al., 2017) in head-fixed mice locomoting on a freely rotating circular treadmill (**Figure 1B; Supplementary Figure 1A,B and Video**). This approach allows Ca^{2+} signals arising in dSPNs to be clearly distinguished

112 from those occurring in tdTomato-negative neurons (**Figure 1C, D**), which are overwhelmingly
113 iSPNs, and which together with dSPNs account for approximately 95% of all striatal neurons in
114 mice (Gerfen & Surmeier 2011).

115 Self-paced forward locomotion was associated with prominent increases in fluorescence in
116 groups of neurons both positive and negative for tdTomato (**Figure 1D**). Population Ca^{2+} signals
117 in tdTomato-positive dSPNs were similar to data obtained using photometry in mice expressing
118 GCaMP6f selectively in dSPNs (**Supplementary Figure 1C, D**). Amongst tdTomato-negative
119 neurons, the vast majority resembled dSPNs in morphology, showed Ca^{2+} transients comparable
120 to those observed in dSPNs (**Figure 1E-G**) and displayed population activity consistent with
121 photometric signals obtained specifically from iSPNs (**Supplementary Figure 1E**), suggesting they
122 represent iSPNs. The remaining tdTomato-negative neurons exhibited Ca^{2+} signals distinct from
123 those observed in dSPNs, including elevated baseline fluorescence (**Supplementary Figure 1G**).
124 These cells likely represent interneurons that sparsely populate the striatum, many of which are
125 tonically active.

126 To validate our classification of tdTomato-negative cells into putative iSPNs and interneurons,
127 we virally expressed GCaMP6f in neurons in a cohort of mice (N = 4) in which iSPNs are selectively
128 labeled with tdTomato (*Adora2a*^{Cre} transgenic mice expressing a Cre-dependent tdTomato
129 reporter, henceforth referred to as *Adora2a*^{tdTomato} mice; see methods; **Supplementary Figure**
130 **1H, I**). Ca^{2+} signals obtained from genetically-identified iSPNs were comparable to those imaged
131 in putative iSPNs in *Drd1a*^{tdTomato} mice. Moreover, the small fraction of cells with elevated
132 baseline fluorescence and distinctive activity patterns were also tdTomato-negative in
133 *Adora2a*^{tdTomato} mice, indicating they are not iSPNs but likely represent interneurons
134 (**Supplementary Figure 1I**). To confirm this assertion, we virally expressed Cre-dependent
135 GCaMP6f in the striatum of *ChAT*^{Cre} mice (N = 2) to directly image Ca^{2+} signals in cholinergic
136 interneurons (**Supplementary Figure 1J-L**). Consistent with prior reports (Howe et al., 2019),
137 cholinergic interneurons exhibited elevated baseline fluorescence and movement-related Ca^{2+}
138 signals distinct from SPNs and similar to those observed in some of the tdTomato-negative cells
139 labeled as putative interneurons in *Drd1a*^{tdTomato} and *Adora2a*^{tdTomato} mice. Importantly, the
140 proportions of imaged neurons assigned to dSPNs, iSPNs and interneurons in *Drd1a*^{tdTomato} and
141 *Adora2a*^{tdTomato} mice were comparable and in agreement with anatomical estimates (**Figure 1H**),
142 further validating our classification criteria. Our imaging approach therefore offers the ability to
143 simultaneously monitor and compare the activity of hundreds of striatal neurons (mean $\pm$ SEM:
144 327 ± 13 per field of view (FOV), range: 131–442) belonging to both direct and indirect pathways
145 with high spatial resolution during a simple behavior.
146

Activity in dSPNs and iSPNs is balanced and concurrent during forward locomotion

We simultaneously imaged dSPNs and iSPNs that displayed Ca^{2+} transients clearly distinguished from baseline and neuropil fluorescence during spontaneously-initiated bouts of forward locomotion (treadmill speed > 0.4 cm/s; see methods) in *Drd1a*^{tdTomato} and *Adora2a*^{tdTomato} mice. Under these conditions, intracellular Ca^{2+} transients are unlikely to reflect individual spikes, but rather bursts of action potentials (Kerr & Plenz 2002; Owen et al., 2018; Parker et al., 2018), which are prevalent during movement execution (Berke et al., 2004; Yin et al., 2009; Fobbs et al., 2020). Consistent with this, the frequency of Ca^{2+} transients in dSPNs and iSPNs was exceedingly low during periods of immobility (treadmill speed < 0.2 cm/s) and rose sharply at movement onset without notable temporal offset between pathways (**Figure 2A-C**). The frequency of Ca^{2+} transients increased similarly in dSPNs and iSPNs in proportion to treadmill velocity, remained elevated throughout locomotor bouts and returned to baseline shortly after movement offset.

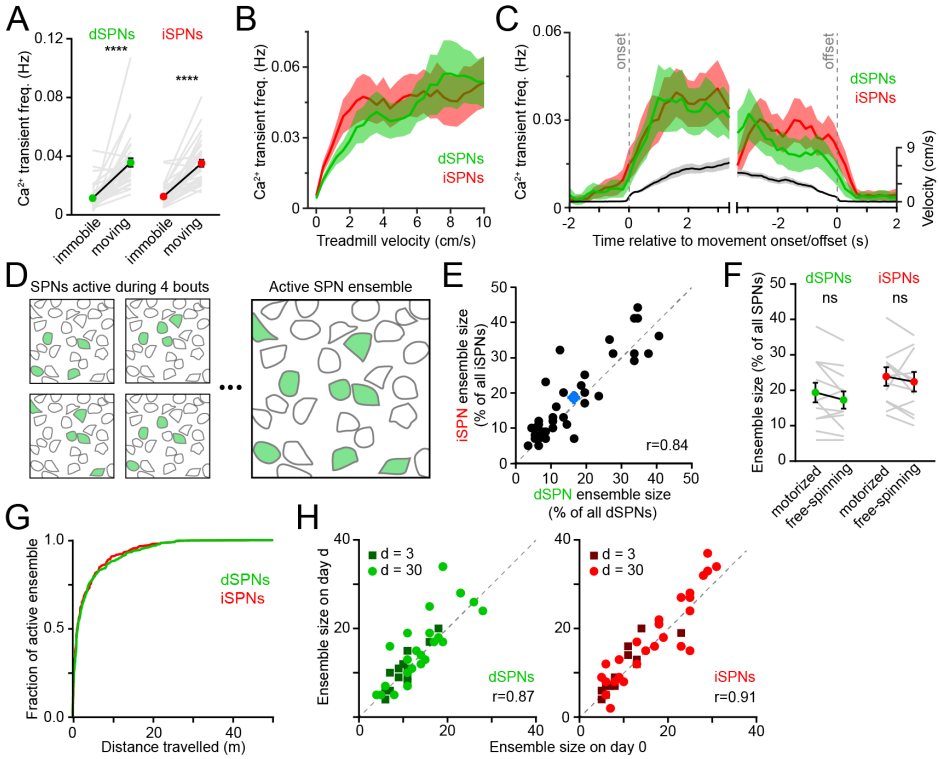

Figure 2. Activity in dSPNs and iSPNs is balanced during forward locomotion

- **A.** Mean Ca^{2+} transient frequency per active dSPNs and iSPNs (n = 38 FOVs in 22 mice) while immobile (light gray) or spontaneously locomoting on treadmill (dark gray; $p = 5.5 \times 10^{-10}$ in dSPNs, 4.1×10^{-10} in iSPNs, Wilcoxon signed-ranks).
- **B.** Mean frequency of Ca^{2+} transients per active dSPN (green) and iSPN (red) at different treadmill velocities. Shaded area: s.e.m.
- **C.** Same as **B** aligned to locomotion onset and offset, overlaid with treadmill velocity (black).
- **D.** Active SPN ensembles comprise all SPNs showing Ca^{2+} transients during forward locomotor bouts. Individual bouts recruit only a subset of SPNs from the overall active ensemble.
- **E.** Size of active dSPN vs. iSPN ensembles, measured as the percentage of all imaged dSPNs or iSPNs exhibiting Ca^{2+} transients per FOV (n = 38 FOVs from 22 mice). Mean ± s.e.m is indicated in blue and unity line in dashed gray. *r*: Spearman correlation coefficient.

Figure 2. (cont'd)

F. Active dSPN (green) and iSPN (red) ensemble size on motorized vs. free-spinning (spontaneously-initiated locomotion) treadmills (n = 12 FOVs; dSPNs: p = 0.23, iSPNs: p = 0.35, Wilcoxon signed-ranks).

G. Cumulative distribution of active dSPNs (green) and iSPNs (red) recruited as a function of distance travelled over the course of imaging sessions.

H. Comparison of the size of dSPN (*left*) and iSPN (*right*) ensembles imaged on separate sessions 3 days (dark dots) or a month (light dots) apart. *r*: Spearman correlation coefficient.

SPNs showing Ca^{2+} elevations during movement formed, over the course of several locomotor bouts, discrete groups, which we termed active SPN ensembles (**Figure 2D**). We quantified the size of active SPN ensembles as the fraction of all imaged dSPNs or iSPNs within a FOV that showed Ca^{2+} transients during forward locomotion over the course of an imaging session. Active dSPN and iSPN ensembles were comparable in size, accounting for (mean $\pm$ s.e.m.) 16.9 $\pm$ 1.8 % and 18.6 $\pm$ 1.8 % of all imaged dSPNs and iSPNs, respectively (**Figure 2E**). For each 2 s of locomotion, approximately 10% of the overall active ensemble displayed Ca^{2+} transients. Individual dSPNs and iSPNs were not systematically active across different locomotor bouts, at particular phases within movement bouts or at specific treadmill velocities, consistent with a sparse sensorimotor code in dorsolateral striatum (Barbera et al., 2016; Klaus et al., 2017; Markowitz et al., 2018). Importantly, the overall size of movement-related ensembles was not limited by distance travelled or the duration of imaging sessions, as their extent was largely captured within the first few locomotor bouts and similar values were obtained using motorized treadmills that imposed a fixed number of running bouts (**Figure 2F, G**). Ensembles were also comparable in size over time, whether imaged a few days or a month apart (**Figure 2H**). Thus, the overall activity of direct and indirect pathway SPNs – as measured by the frequency of Ca^{2+} transients exhibited by individual neurons and the total number of active cells detected over an imaging session (i.e. active SPN ensembles) – is balanced, with few notable differences distinguishing dSPNs from iSPNs during self-paced forward locomotion.

Reducing DA receptor signaling modulates the size of active SPN ensembles

DA receptor signaling is thought to modulate the firing rate of SPNs. Whether it also modulates the size of SPN ensembles representing motor actions is not known. We can conceive of two scenarios: if SPN ensembles are primarily defined anatomically by excitatory afferent connectivity, DA may alter SPN firing rates with minimal changes in ensemble size (**Figure 3A**). If, on the other hand, the extent of SPN ensembles is determined functionally by the potency of excitatory afferents and/or the excitability of SPNs, DA may exert a strong influence on ensemble size in addition to firing rates (**Figure 3B**). To distinguish between these possibilities, we first compared Ca^{2+} signals in dSPNs and iSPNs before and after systemic administrations of a cocktail of D_1 and D_2 receptor ($D_{1/2}R$) antagonists. Although this manipulation did not impact the velocity

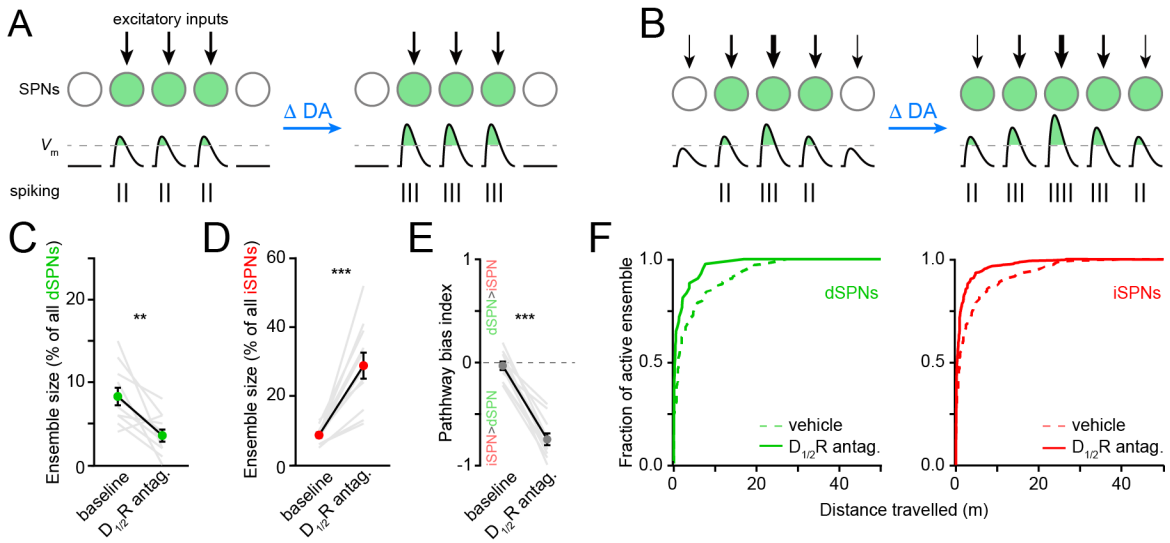

Figure 3. Reducing DA receptor signaling expands iSPN ensembles and shrinks dSPN ensembles.

A,B. DA may affect SPN firing rates without (**A**) or with (**B**) accompanying changes in active ensemble size. Active SPNs are depicted as filled circles. Movement-related excitatory inputs of varying strength (arrows) evoke action potentials (vertical bars) when postsynaptic membrane depolarizations exceed spike threshold (dashed line). In this example, changes in extracellular DA increase the strength of excitatory afferents and/or the intrinsic excitability of SPNs.

C. Percentage of all imaged dSPNs showing Ca^{2+} transients during locomotion before and after systemic administration of $D_{1/2}$R antagonists (n = 11 FOVs in 5 mice, p = 0.003 vs. baseline, Wilcoxon signed-rank). Mean ± s.e.m are overlaid.

D. Same as **C** for iSPNs (p = 0.001 vs. vehicle, Wilcoxon signed-rank).

E. Bias in the size of active dSPN and iSPN ensembles before and after $D_{1/2}$R antagonist treatment (p = 0.001 vs. baseline, Wilcoxon signed-rank).

F. Cumulative distribution of active dSPNs (*left*) and iSPNs (*right*) recruited as a function of distance travelled in vehicle- (dashed) and $D_{1/2}$R antagonist-treated mice (solid).

or duration of locomotor bouts on the treadmill, it curtailed the total number of bouts that mice spontaneously initiate compared to vehicle-treated animals (**Supplementary Figure 2A-C**). We therefore limited our analyses to imaging sessions on motorized treadmills to encourage locomotion and to maintain locomotor speed and distance traveled constant.

The total number of SPNs recruited by forward locomotion was significantly altered in mice treated with $D_{1/2}$R antagonists compared to vehicle-treated controls (**Figure 3C, D**). Blocking DA receptors shrunk active dSPN ensembles by half (p = 0.006, Mann-Whitney; vehicle: n = 10 FOVs in 5 mice; DA antagonist: n = 11 FOVs in 5 mice), and expanded iSPN ensembles more than three-fold (p = 5.7 x 10^{-6}, Mann-Whitney), resulting in a strong imbalance in favor of the indirect pathway (p = 5.7 x 10^{-6}, Mann-Whitney; **Figure 3E**). This apparent dichotomous modulation is not secondary to changes in the likelihood that Ca^{2+} transients are detected in dSPNs and iSPNs. Indeed, the mean amplitude of Ca^{2+} transients in dSPNs and iSPNs remained unchanged (**Supplementary Figure 2G-I**), and the frequency of Ca^{2+} events recorded increased in both pathways, although it only reached statistical significance in iSPNs (p = 0.007; Mann-Whitney vs.

205 vehicle; **Supplementary Figure 2E**). Moreover, the extent of active ensembles was fully captured
206 well before the end of imaging sessions (**Figure 3F**). These data therefore indicate that reducing
207 DA signaling evokes substantial reconfiguration of the overall number of dSPNs and iSPNs
208 associated with forward locomotion within minutes, and suggests that, under baseline
209 conditions, DA continuously promotes the activation of dSPNs and represses iSPNs to maintain
210 balance between pathways.
211
212 **Elevating DA reconfigures active SPN ensembles in a concentration-dependent manner**
213 Given the marked effects of $D_{1/2}R$ antagonists on SPN ensemble size, we next investigated
214 whether increasing DA signaling would exert the opposite effect. We hypothesized that dSPN
215 ensembles would grow in size with rising DA, whereas iSPNs would be insensitive (Iino et al.,
216 2020; Lee et al., 2020). To test this, we imaged striatal activity upon concomitant
217 pharmacological stimulation of D1 and D2 receptors (n = 20 FOVs in 14 mice) while mice
218 locomoted on motorized treadmills to mitigate effects on spontaneous behavior (**Supplementary**
219 **Figure 3A-C**). We examined the response of dSPNs and iSPNs to increasing concentrations of
220 $D_{1/2}R$ agonists (0.3, 1, 3 and 6 mg/kg; delivered i.p.) in comparison to vehicle treatment.

221 Stimulating DA receptors markedly altered the size of SPN ensembles associated with forward
222 locomotion, yielding a dose-dependent imbalance in favor of the direct pathway ($p = 2.1 \times 10^{-5}$,
223 Kruskal-Wallis test; **Figure 4B**). However, the effects on dSPN and iSPN ensembles underlying
224 this bias varied with DA receptor agonist dose. At low concentrations (0.3-1 mg/kg), iSPN
225 ensembles remained unchanged, whereas dSPN ensembles were either unchanged or larger, in
226 agreement with our working hypothesis. At higher concentrations (3-6 mg/kg), $D_{1/2}R$ agonists
227 promoted a striking decline in the prevalence of both active dSPNs and iSPNs, with iSPNs showing
228 the strongest decrease. The drop in the number of active iSPNs suggest that iSPNs are not
229 maximally repressed by baseline DA tone *in vivo* (Marcott et al., 2014). The reduction in the size
230 of active dSPN ensembles was not expected. It did not stem from insufficient sampling of SPN
231 activity during our imaging session (**Figure 4C**), or from differences in our ability to detect Ca^{2+}
232 events, as DA does not affect somatodendritic Ca^{2+} transients in dSPNs (Day et al., 2008), and the
233 amplitude and frequency of Ca^{2+} transients were not reduced (**Supplementary Figure 3D, E**).

234 Although DA receptors are strongly expressed in striatum, we cannot exclude the possibility
235 that systemic administration of DA receptor agonists impact striatal activity indirectly, especially
236 at high doses. We therefore investigated how movement-related SPN ensembles are affected by
237 manipulations that preferentially elevate endogenous DA levels in striatum. We first considered
238 the effects of natural rewards, which are well established to elevate extracellular DA throughout
239 striatum (**Figure 4D**), and which were recently shown to elevate protein kinase A activity in dSPNs
240 for 10s of seconds (Lee et al., 2020). To do so, we imaged striatal activity in a cohort of water-
241 restricted mice locomoting on a motorized treadmill before and after delivering water rewards.

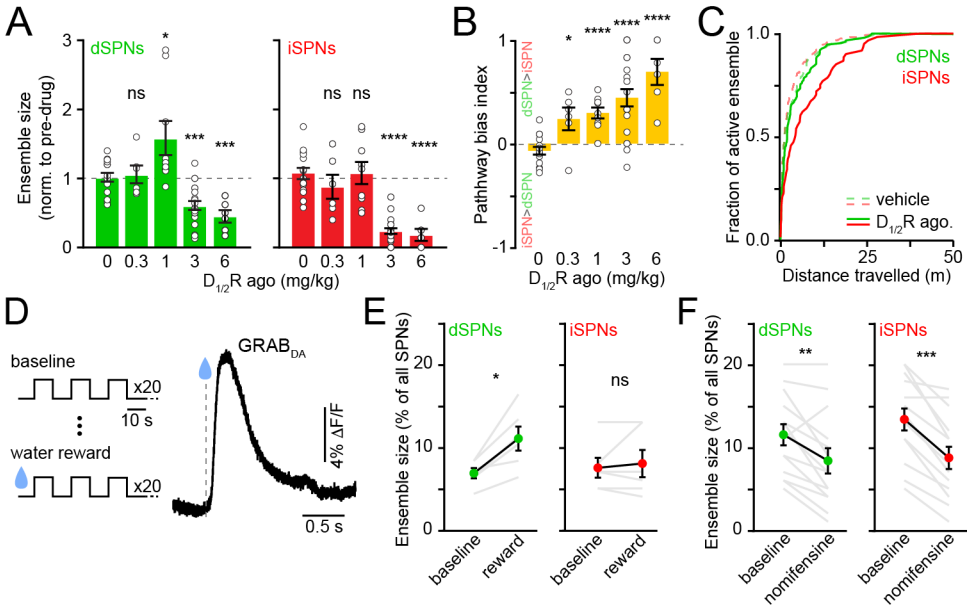

Figure 4. Elevating DA receptor signaling reconfigures movement-related SPN ensembles in a concentration-dependent manner

A. Fraction of imaged dSPNs (*left*, green) and iSPNs (*right*, red) active during locomotion in mice treated with increasing concentrations of $D_{1/2}R$ agonists normalized to pre-drug baseline (vehicle, n = 15 FOVs; 0.3 mg/kg: n = 6 FOVs, dSPN p = 0.92, iSPN p = 0.27; 1 mg/kg: n = 9 FOVs, dSPN p = 0.04, iSPN, p = 0.92; 3 mg/kg: n = 20 FOVs, dSPN p = 1.7 x 10^{-4}, iSPN p = 3.1 x 10^{-9}; 6 mg/kg: n = 6 FOVs, dSPN p = 2.9 x 10^{-4}, iSPN p = 3.7 x 10^{-5}; all vs. vehicle, Mann-Whitney).

B. Bias in ensemble size between dSPNs and iSPNs (0.3 mg/kg: p = 0.02; 1 mg/kg: p = 4.3 x 10^{-5}; 3 mg/kg: p = 7.8 x 10^{-6}; 6 mg/kg: p = 7.4 x 10^{-5}; all vs. vehicle, Mann-Whitney).

C. Cumulative distribution of active dSPNs (green) and iSPNs (red) recruited with travelled distance after systemic administration of vehicle (dashed) and $D_{1/2}R$ agonists (solid).

D. *Left*, experimental paradigm: mice execute blocks of three 10 s-long locomotor bouts on a motorized treadmill. The first 20 blocks are unrewarded (baseline); the following 20 are preceded by delivery of a water reward. *Right*, example $GRAB_{DA2h}$ fluorescence (Sun et al., 2020) imaged from dorsolateral striatum using fiber photometry upon water reward delivery. *Inset*, mean ± s.e.m $GRAB_{DA}$ transient amplitude (n = 5 mice).

E. dSPN (*left*) and iSPNs (*right*) ensemble size (percentage of imaged neurons active per FOV) imaged during baseline and rewarded blocks (n = 6 FOVs in 4 mice; dSPN p = 0.03, iSPN p > 0.9, all vs. baseline, Wilcoxon signed-ranks). Mean ± s.e.m overlaid for each group.

F. Same as **e** after treatment with the DA transporter inhibitor nomifensine (n = 14 FOVs in 6 mice; dSPN p = 0.005, iSPN p = 2.4 x 10^{-4}, all vs. baseline, Wilcoxon signed-ranks).

Water delivery selectively increased in the number of active dSPNs (**Figure 4E**) without altering Ca^{2+} transient properties (**Supplementary Figure 3F, G**), similar to results obtained with low concentrations of $D_{1/2}R$ agonists (**Figure 4A**).

We also considered the effects of membrane DA transporter (DAT) inhibition. Presynaptic reuptake of DA into axonal terminals is the primary mechanism through which DA neurons limit the amplitude and duration of DA transients in the striatum, and inhibiting DAT leads to strong and prolonged elevations in extracellular DA in striatum (Sulzer et al., 2016). We therefore compared the number of active SPNs before and after systemic administration of a related DAT

250 antagonist: nomifensine. We observed effects similar to those reported with higher $D_{1/2}R$ agonist
251 concentrations (**Figure 4A**), as nomifensine significantly decreased the size of active ensembles
252 in both dSPNs and iSPNs (**Figure 4F**; **Supplementary Figure 3H, I**). These data therefore indicate
253 that the size of SPN ensembles recruited during forward locomotion is susceptible to modulation
254 by rising DA, but that elevated extracellular DA levels are not invariably associated with
255 proportional increases in the number of active dSPNs. Instead, dSPNs follow an 'inverted-U'
256 shaped function, where too little or too much DA negatively impacts the size of their action-
257 related ensemble.
258
259 **Chronic DA depletion selectively limits the size of active dSPN ensembles**
260 The degeneration of substantia nigra pars compacta (SNc) DA neurons in animal models of
261 Parkinson's disease evokes imbalances in activity rates in dSPNs and iSPNs (Parker et al., 2018;
262 Ryan et al., 2018). To examine whether chronic loss of DA also evokes changes in the size of
263 active SPN ensembles, we injected the neurotoxin 6-hydroxydopamine (6-OHDA) into the SNc
264 ipsilateral to the striatal hemisphere under investigation in a subset of mice (N = 12). This
265 manipulation causes DA neurons to degenerate (**Figure 5B, C; Supplementary Figure 4A-D**) and
266 produces mild motor impairments as early as 24 hours – and for up to a month – after lesion
267 (**Supplementary Figure 4E-H**). Importantly, unlike the profound akinesia that results from
268 bilateral DA denervation, hemi-lesioned mice continue to spontaneously engage in locomotor
269 behavior, permitting the study of movement-related SPN activity within dorsolateral in the
270 absence of DA. A separate cohort of mice (N = 6) was treated identically, except that 6-OHDA
271 was omitted from the injection solution (sham group). These mice did not exhibit differences in
272 the density of DA neuron cell bodies in SNc or of axons in striatum (**Figure 5C; Supplementary**
273 **Figure 4C,D**), or in striatal Ca2+ activity (**Figure 5D-F; Supplementary Figure 4K-N**).

274 Lesioning DA neurons had a strong, time-dependent effect on the size of dSPN (two-way
275 ANOVA lesion x time: $F_{2,53} = 3.66$, $p = 0.03$; **Figure 5D**) and iSPN ensembles associated with
276 forward locomotion ($F_{2,53} = 11.92$, $p = 5.3 \times 10^{-5}$; **Figure 5E**), resulting in a pronounced imbalance
277 between pathways ($F_{2,53} = 19.0$, $p = 6.1 \times 10^{-7}$; **Figure 5F**). Within the first 24 h, the number of
278 dSPNs displaying Ca^{2+} transients was halved, whereas active iSPNs within the same FOV more
279 than doubled in number. These effects, which were similar to those observed with DA receptor
280 antagonists (**Figure 3C-E**), were present at all recorded velocities (**Figure 5G**), as well as on a
281 motorized treadmill (**Supplementary Figure 4I**). In addition, they were not associated with
282 significant changes in either amplitude or frequency of Ca^{2+} transients in active SPNs
283 (**Supplementary Figure 4M, N**), excluding differences in behavior and signal detection as likely
284 confounds. DA denervation therefore rapidly alters the size of dSPN and iSPN ensembles,
285 generating a strong imbalance in favor of the indirect pathway.

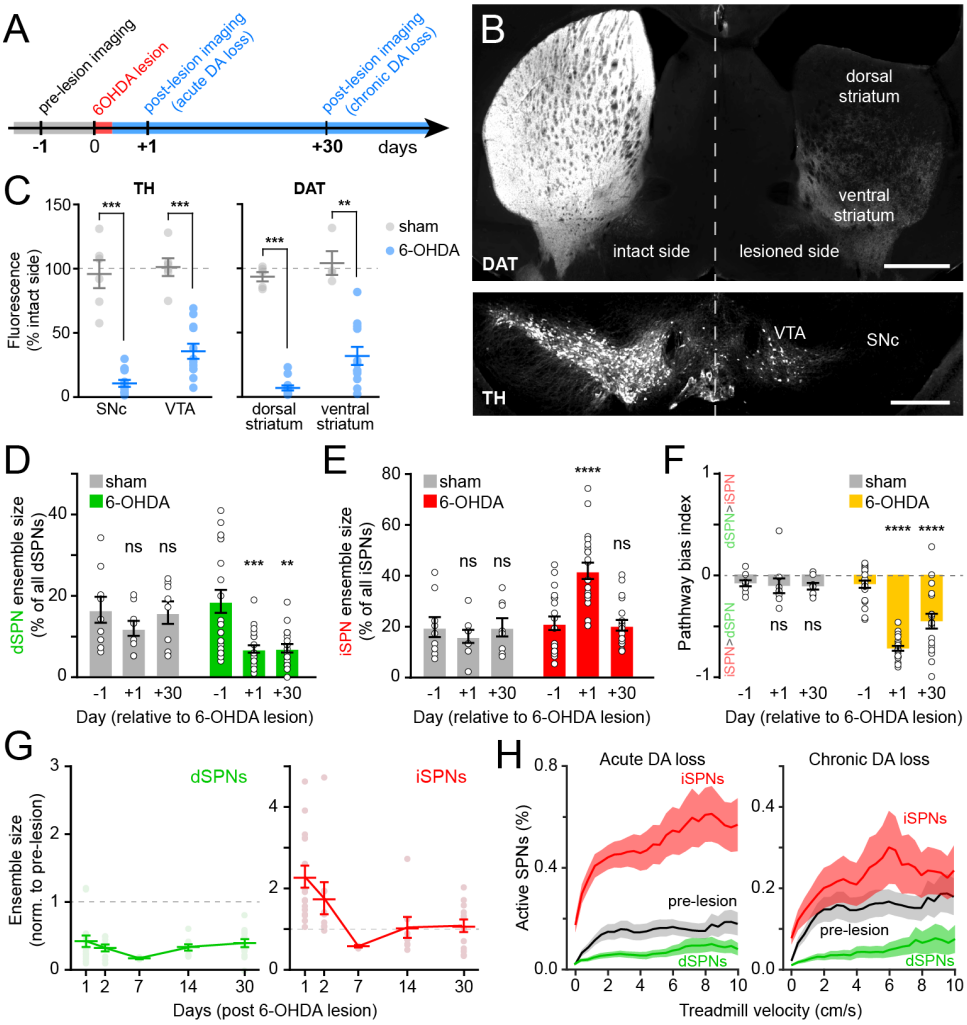

Figure 5. Chronic DA neuron lesions impair dSPN ensembles.

A. Experimental timeline relative to unilateral lesion of SNc DA neurons.

B. Example coronal forebrain (*top*) and ventral midbrain (*bottom*) sections from a mouse injected with 6-OHDA into the right SNc and stained for DAT (*top*) and TH (*bottom*). VTA, ventral tegmental area. Scale bars: 1 mm (*top*), 0.5 mm (*bottom*).

C. Immunofluorescence signal for TH in SNc and VTA (*left*) and DAT in dorsal and ventral striatum (*right*) on the treated side normalized to the intact side in sham- (gray; n = 6) and 6-OHDA-lesioned mice (blue; n = 12). Mean ± s.e.m is overlaid. Asterisks depict significant difference from sham (SNc $p = 1.1 \times 10^{-4}$; VTA $p = 1.1 \times 10^{-4}$; dorsal striatum $p = 3.2 \times 10^{-4}$; ventral striatum $p = 0.001$; Mann-Whitney).

D. Size of dSPN ensembles before (day -1), immediately after (day +1) or a month after (day +30) sham (n = 9 FOVs in 6 mice; day 1 $p = 0.42$; day 30 $p > 0.9$) or 6-OHDA-mediated SNc lesions (n = 21 FOVs from 12 mice; day 1 $p = 1.8 \times 10^{-4}$; day 30 $p = 0.001$, all vs. pre-lesion, post-hoc Bonferroni).

E. Same as **D** for iSPNs (Sham: day 1 $p = 0.78$; day 30 $p > 0.9$; 6-OHDA: day 1 $p = 8.0 \times 10^{-7}$, day 30 $p > 0.9$, all vs. pre-lesion, post-hoc Bonferroni).

F. Bias in ensemble size between dSPNs and iSPNs (sham: day 1 $p > 0.9$; day 30 $p > 0.9$; 6-OHDA: day 1: $p = 3.1 \times 10^{-14}$, day 30: $p = 4.2 \times 10^{-5}$, all vs. pre-lesion, post-hoc Bonferroni).

G. Percentage of imaged dSPNs (green) and iSPNs (red) displaying Ca^{2+} transients in 200 ms-time bins vs. treadmill velocity during self-initiated forward locomotion on day 1 (*left*, acute DA loss) or day 30 (*right*, chronic DA loss) after 6-OHDA lesion. Pre-lesion values for dSPNs and iSPN combined is shown in black.

286 **H.** Movement-related dSPN (*left*, green) and iSPN (*right*, red) ensemble size imaged on different days after SNc lesions with 6-OHDA normalized to pre-lesion ensemble size (n = 16, 9, 2, 8 and 14 FOVs on days 1, 2, 7, 14 and 30). Note that iSPNs return to baseline values within the first two weeks post-lesion.

287 To determine if homeostatic adaptations that accompany chronic DA denervation impact SPN
288 ensembles, we also imaged striatal activity in the same cohort of mice 30 days later. Although
289 the number of dSPNs recruited during forward locomotion remained depressed, the expansion
290 of iSPN ensembles observed immediately after 6-OHDA treatment was no longer evident (**Figure**
291 **5D-F**). Instead, active iSPN ensembles returned to pre-lesion levels within a few days (**Figure 5G**).
292 As with imaging sessions on day 1, we confirmed that the selective defect in dSPNs on day 30 was
293 present across treadmill velocities (**Figure 5H**), that it was maintained on a motorized treadmill
294 (**Supplementary Figure 4I**), and that it was not associated with differences our ability to detect
295 Ca^{2+} transients or adequately capture the extent of active SPN ensembles (**Supplementary Figure**
296 **4J, M, N**). Despite compensatory changes in iSPNs, the overall size of SPN ensembles recruited
297 over the course of imaging sessions remained significantly biased towards the indirect pathway
298 in chronically lesioned mice (**Figure 5F**). These results therefore indicate that DA depletion
299 strongly biases striatal activity towards the indirect pathway both acutely and chronically, and
300 point to plasticity mechanisms that normalize the number of active iSPNs, but not dSPNs, upon
301 persistent absence of DA signaling
302
303 **Chronic DA depletion alters how SPN ensembles respond to DA**
304 Motor impairments in Parkinson's disease are typically managed by elevating striatal DA with
305 L-DOPA, the metabolic precursor for DA. However, as the disease progresses and SNc
306 degeneration becomes more severe, L-DOPA evokes abnormal involuntary movements, or
307 dyskinesias, that severely diminish quality of life (Cenci 2014; Picconi et al., 2018). We therefore
308 investigated whether DA's influence on SPN ensembles changes in the striatum of mice in which
309 DA axons are chronically lost. To do this, we first treated mice that had received unilateral 6-
310 OHDA infusions in SNc at least one month earlier with a single dose of L-DOPA. As expected, this
311 treatment reversed the turning bias of lesioned mice within minutes (**Supplementary Figure 5A**).
312 L-DOPA also affected SPN ensembles, albeit to a much greater extent than that observed with
313 $D_{1/2}R$ agonists in DA-intact animals. The number of dSPNs exhibiting Ca^{2+} transients during
314 forward locomotion on motorized treadmills in DA-lesioned mice expanded by 10-fold with L-
315 DOPA, outnumbering pre-lesion dSPN ensembles by a factor of two on average and reaching
316 upwards of 70% of all imaged dSPNs in some fields of view (**Figure 6A, B**). In addition, the overall
317 number of active iSPNs decreased below pre-lesion levels (**Figure 6C**), further contributing to
318 biasing ensembles in DA-depleted mice towards the direct pathway (**Figure 6D**). These
319 population-level effects are unlikely to stem from changes in the likelihood of detecting Ca^{2+}
320 transients in active SPNs (**Supplementary Figure 5B**).

321 These results indicate that L-DOPA exerts a stronger positive modulatory influence on dSPNs
322 in DA-depleted mice than $D_{1/2}R$ agonists do in DA-intact mice, leading to excessive recruitment
323 of dSPNs not normally associated with forward locomotion. This discrepancy may stem from
324 changes in how striatal circuits respond to DA following SNc neuron loss, or from differences in

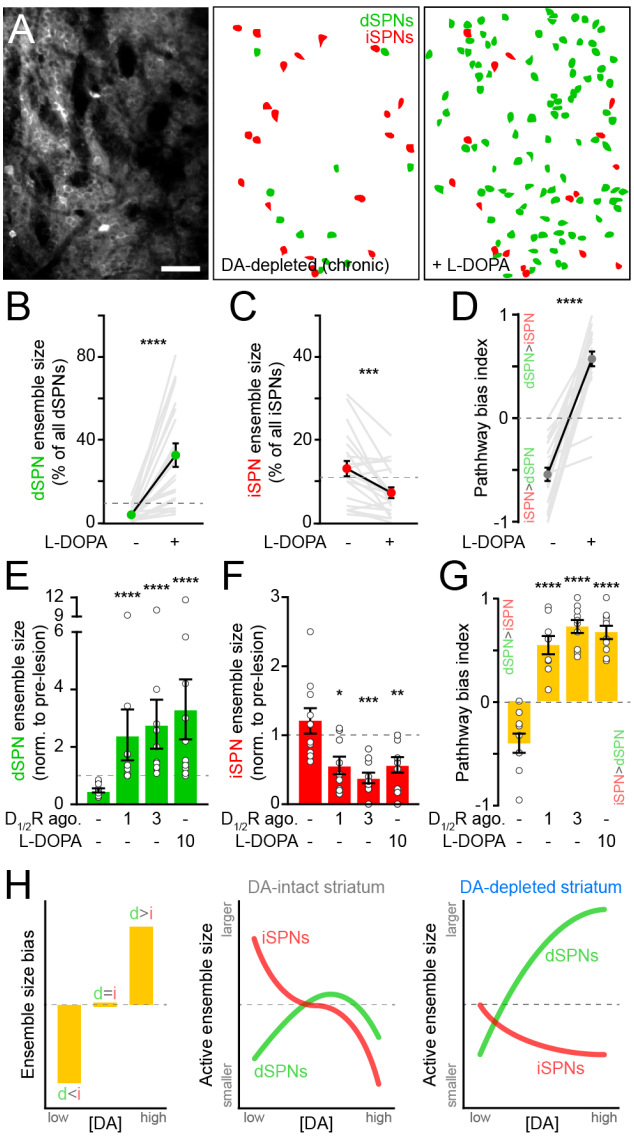

Figure 6. SPN ensembles respond differently to DA after chronic DA depletion

- **A.** Maximum projection image of a chronically DA-depleted dorsolateral striatum (*left*) and spatial distribution of dSPNs (green) and iSPNs (red) active ensembles imaged immediately before (*middle*) and during (*right*) systemic administration of L-DOPA. Scale bar: 50 μm.
- **B.** Movement-related dSPN ensemble size in chronically-lesioned mice before and after elevating striatal DA with L-DOPA (n= 21 FOVs in 12 mice; $p = 1.9 \times 10^{-6}$, Wilcoxon signed rank). Dashed line indicates the mean size of dSPN ensembles prior to 6-OHDA lesion.
- **C.** Same as **B** for iSPNs (n= 21 FOVs in 12 mice; $p = 7.0 \times 10^{-4}$, Wilcoxon signed rank).
- **D.** Bias in the size of active dSPN and iSPN ensembles before and after L-DOPA treatment (n= 21 FOVs in 12 mice; $p = 9.5 \times 10^{-7}$, Wilcoxon signed rank).
- **E.** Movement-related dSPN ensemble size in chronically-lesioned mice (n = 10 FOVs in 7 mice) imaged before (baseline) and after systemic administration (on separate sessions) of $D_{1/2}R$ agonists at different concentrations (1 mg/kg: $p = 2.2 \times 10^{-5}$; 3 mg/kg: $p = 1.1 \times 10^{-5}$, all vs. baseline, Mann-Whitney) and L-DOPA ($p = 1.1 \times 10^{-5}$ vs. baseline, Mann-Whitney) normalized to the size of active dSPN ensembles prior to 6-OHDA lesion. Dashed line indicates unity.

325

Figure 6. (Cont'd)

F. Same as **E** for iSPNs (n = 10 FOVs in 7 mice; 1 mg/kg: p = 0.01; 3 mg/kg: p = 1.3 x 10^{-4}; L-DOPA: p = 8.4 x 10^{-3}; all vs. baseline, Mann-Whitney).

G. Bias in the size of active dSPN and iSPN ensembles before and after treatment with $D_{1/2}$R agonists or L-DOPA (n = 10 FOVs in 7 mice; 1 mg/kg: p = 2.2 x 10^{-5}; 3 mg/kg: p = 1.1 x 10^{-5}; L-DOPA, p = 1.1 x 10^{-5}; all vs. baseline, Mann-Whitney).

H. Diagrams summarizing observed changes in the overall balance between dSPN and iSPN ensembles (*left*) and the specific changes in the size of movement-related dSPN (green) and iSPN (red) ensembles with varying DA levels in the striatum of intact (*middle*) and DA-depleted mice (*right*).

the pharmacological potency of these treatments. Indeed, L-DOPA's ability to elevate extracellular DA varies strongly with DA axonal density, producing disproportionately high and prolonged increases in DA in the striatum of DA-lesioned animals (Abercrombie et al., 1990). To distinguish between these possibilities, we directly compared the effects of L-DOPA and $D_{1/2}$R agonists on SPN ensembles in a subset of DA-depleted mice locomoting on motorized treadmills. $D_{1/2}$R agonists no longer provoked a decline in the number of active dSPNs in chronically lesioned mice as they did in DA-intact mice, even at high concentrations. Instead, forward locomotion recruited twice as many dSPNs as it did pre-lesion (**Figure 6E**). This expansion was comparable in magnitude to L-DOPA's, indicating that dSPNs ensembles in DA-depleted mice respond differently to DA than in intact-mice. $D_{1/2}$R agonists also mimicked the effects of L-DOPA on iSPNs, cutting the number of active cells in half (**Figure 6F**). At all doses tested, $D_{1/2}$R stimulation evoked a strong imbalance in favor of the direct pathway (**Figure 6G**). These data therefore indicate that DA signaling favors the recruitment of dSPNs relative to iSPNs in both DA-intact and DA-depleted mice, but that the underlying population dynamics differ profoundly (**Figure 6H**). Whereas dSPN ensembles are kept small with increasing DA under basal conditions, they are unrestrained in chronically lesioned mice and susceptible to dramatic expansion. At the same time, DA signaling depresses the size of iSPN ensembles, even at low levels.

DISCUSSION

In this study, we sought to reveal how acute and prolonged manipulations of DA signaling impact striatal output. To do so, we monitored intracellular Ca^{2+} signals in dSPNs and iSPNs simultaneously using two-photon microscopy to permit the identification of subtle imbalances between direct and indirect pathways long proposed to lie at the heart of basal ganglia function and dysfunction (Nelson & Kreitzer 2014; Klaus et al., 2019). We specifically examined changes in the size of SPN ensembles recruited during a low-dimensional locomotor behavior to facilitate comparisons across imaging sessions.

354 There is compelling evidence, primarily in *ex vivo* brain slices, that DA modulates the intrinsic
355 excitability of SPNs and the strength of excitatory afferents to promote the activation of dSPNs
356 and impede that of iSPNs. The net consequences of DA's actions on SPNs *in vivo* have almost
357 exclusively been understood in the context of firing rates. Although this view finds experimental
358 support (Mallet et al., 2006; Ryan et al., 2018), it does not speak to other aspects of striatal
359 activity that DA may modulate, such as bursting or population dynamics. Our results suggest that
360 DA exerts a strong influence on the size of movement-related SPN ensembles in ways not
361 captured by existing models of DA function.

362 Reducing DA signaling causes a strong population-level imbalance in favor of the indirect
363 pathway by simultaneously depressing the number of dSPNs and doubling the number of iSPNs
364 displaying movement-related Ca^{2+} transients. This effect is unlikely to stem from differential
365 modulation of voltage-gated Ca^{2+} channels (Day et al., 2008; Tritsch & Sabatini 2012) or excitatory
366 afferents, which are largely shared between pathways (Kress et al., 2013; Wall et al., 2013; Guo
367 et al., 2015). Indeed, we did not detect imbalances in either the amplitude or frequency of Ca^{2+}
368 transients in dSPNs and iSPNs. Instead, the observed ensemble changes support the view that,
369 despite differences in the apparent affinity of D_1 and D_2 receptors for DA, basal DA levels promote
370 the recruitment of dSPNs and limit that of iSPNs. The latter is consistent with the recent
371 observation that protein kinase A is strongly activated in iSPNs in response to phasic dips in
372 extracellular DA (Lee et al., 2020). Thus, periods of diminished DA signaling (i.e. following
373 negative reward prediction errors) may be associated with a coincident expansion and reduction
374 in the number of iSPNs and dSPNs responding to shared excitatory inputs with somatodendritic
375 Ca^{2+} transients, respectively.

376 Elevating DA signaling also affects SPN ensembles, promoting a dose-dependent imbalance
377 toward the direct pathway. However, the changes underlying this bias vary with DA levels. Mild
378 increases in DA signaling with $D_{1/2}R$ agonists or natural rewards selectively increases the size of
379 dSPN ensembles, indicating that dSPNs remain sensitive to phasic elevations in DA. By contrast,
380 boosting endogenous DA to levels with nomifensine or $D_{1/2}R$ agonists similar to what may be
381 experienced with stimulants like methylphenidate in the treatment of attention deficit
382 hyperactivity disorder causes both dSPN and iSPN ensembles to shrink. Although we cannot
383 exclude the possibility that the observed effects reflect DA's extra-striatal actions, the fact that
384 DA axons project most densely to striatum, that DA receptors are strongly expressed in striatum,
385 and that distinct manipulations produce similar phenotypes suggest that SPN ensemble size may
386 be directly modulated by striatal DA receptors. Our results fundamentally challenge the
387 pervasive notion that high DA invariably promotes the activation of dSPNs, and invites a more
388 cautious interpretation of the effects of these drugs on striatal circuits and behavior. In line with
389 this, several electrophysiological studies have reported that D_1R agonists can suppress voltage-
390 gated Na^+ channels and SPN firing (Akaike et al., 1987; Calabresi et al., 1987; Schiffmann et al.,

391 1995; Hernandez-Lopez et al., 1997; Kravitz et al., 2010; Planert et al., 2013). The observation
392 that iSPNs are capable of detecting and responding to additional DA and D_2R signaling from
393 baseline tonic levels is also consistent with prior work in brain slices (Marcott et al., 2014).
394 Collectively, our data show that the size of iSPN ensembles is inversely related to extracellular
395 DA levels, whereas dSPN ensembles follow an 'inverted-U' shaped response with limited capacity
396 for expansion with increasing DA. Interestingly, a similar relationship has been described in
397 prefrontal cortex with DA acting on D_1Rs to regulate cognitive functions like working memory
398 (Vijayraghavan et al., 2007), pointing to a common mechanism of dopaminergic modulation
399 across brain regions.

400 It is increasingly recognized that motor impairments in Parkinson's disease reflect aberrant
401 activity patterns within the basal ganglia that arise not only from the loss of striatal DA, but also
402 from subsequent homeostatic circuit adaptations (Zhai et al., 2019). Indeed, we observed stark
403 differences in the activity of iSPNs after acute and prolonged depletion of DA. Whereas iSPNs
404 initially respond to sudden DA loss with a surge in active cells similar to that evoked with $D_{1/2}R$
405 antagonists, movement-related iSPN ensembles returned to their pre-lesion size within a week.
406 This observation agrees with recent work showing that persistent DA depletion in mouse models
407 of Parkinson's disease does not evoke excessive disinhibition of the indirect pathway (Ketzef et
408 al., 2017; Parker et al., 2018; Ryan et al., 2018). Our results indicate that iSPNs possess a
409 remarkable capacity for homeostatic plasticity, which may stem from dendritic atrophy, spine
410 loss, elevated inhibition from surrounding interneurons and diminished intrinsic excitability upon
411 DA depletion (Gittis & Kreitzer 2012; Zhai et al., 2019). By contrast, dSPN ensembles failed to
412 functionally recover from acute loss of DA, as the number of active dSPNs remained low for up
413 to a month after 6-OHDA infusion, despite reported increases in intrinsic excitability (Fieblinger
414 et al., 2014; Ketzef et al., 2017). This finding echoes a previous report that many dSPNs are
415 electrically silent in lesioned animals and more difficult to evoke spikes from (Mallet et al., 2006),
416 possibly because DA depletion also weakens excitatory synapses (Fieblinger et al., 2014; Parker
417 et al., 2016; Ketzef et al., 2017) and potentiates GABAergic influences onto dSPNs (Lemos et al.,
418 2016). Thus, the bradykinesia that defines Parkinson's disease may result not only from the
419 elevated discharge of iSPNs during periods of immobility (Parker et al., 2018; Ryan et al., 2018),
420 but also from the diminished ability to recruit large populations of dSPNs during movement.

421 DA replacement therapy with L-DOPA is the main line of treatment for Parkinson's disease.
422 Though effective at alleviating motor impairments early in disease, L-DOPA eventually evokes
423 dyskinesias. These abnormal involuntary movements are believed to arise in part from striatal
424 circuit maladaptation to DA denervation beyond a critical threshold (Cenci 2014; Picconi et al.,
425 2018). In our 6-OHDA-lesioned animals – which model the severe SNc degeneration of advanced
426 Parkinson's disease – restoring DA signaling with L-DOPA or $D_{1/2}R$ agonists reconfigures SPN
427 ensembles to an extent not seen in DA-intact mice. Specifically, active dSPN ensembles no longer

428 showed an 'inverted-U' shaped response to increasing DA. Instead, they grew larger than pre-
429 lesion ensembles, reaching 60-80% of all imaged dSPNs in some preparations. This suggests that,
430 as the disease progresses and DA degeneration worsens, the way in which dSPNs respond to DA
431 fundamentally changes, complicating attempts at restoring balance between striatal pathways
432 using DA. It is possible that the elevated density and sensitivity of DA receptors that accompany
433 severe DA neuron loss (Gerfen 2003) contribute to the population-level phenotypes were
434 observe. The expansion of dSPN ensembles associated with motor actions may gravely
435 compromise the ability of dSPNs to distinctly represent different movements and may help
436 explain why L-DOPA treatment eventually induces uncontrolled choreiform and ballistic
437 movements involving the head, trunk and limbs.

438 It is possible that the changes in ensemble size we reveal here reflect DA's well-established
439 influence on SPN intrinsic excitability and firing rates (**Figure 3A, B**). The high degree of
440 divergence and convergence of excitatory inputs to striatum (Flaherty & Graybiel 1994; Reig &
441 Silberberg 2014; Mandelbaum et al., 2019) may allow DA's effects on intrinsic excitability,
442 excitatory afferent strength and firing rates to translate into a population code, effectively
443 amplifying DA's impact on basal ganglia nuclei downstream of striatum. Alternatively, DA may
444 independently regulate the likelihood that SPNs respond to excitatory inputs with
445 somatodendritic Ca^{2+} spikes, a key element governing plasticity across brain areas in health and
446 disease (Lerner & Kreitzer 2011; Zhuang et al., 2013; Bittner et al., 2017; Nanou & Catterall 2018).
447 Ca^{2+} elevations in SPNs are tightly correlated with bursts of action potentials (Kerr & Plenz 2002;
448 Owen et al., 2018) and can be modulated by local interneurons independent of firing rate (Owen
449 et al., 2018). Thus, intracellular Ca^{2+} signals may not reflect firing rates as much as the propensity
450 of SPNs to emit bursts of action potentials. As such, fluorescent Ca^{2+} transients in SPNs constitute
451 a measure of striatal activity in their own right, highlighting bursting events likely to impact Ca^{2+}-
452 dependent synaptic plasticity in SPNs (Carter & Sabatini 2004; Jedrzejewska-Szmek et al., 2017).
453 In addition to its established role in shaping plasticity at individual synapses (Calabresi et al.,
454 2007; Pawlak & Kerr 2008; Shen et al., 2008), DA may therefore also regulate the number of
455 neurons eligible to participate in such plasticity.

456 Several of our manipulations did not modify the frequency of Ca^{2+} transients oppositely in
457 dSPNs and iSPNs. We interpret this to mean that the factors that drive Ca^{2+} transients in SPNs
458 (e.g. trains of excitatory inputs) are shared between pathways and not subject to strong pathway-
459 specific modulation by DA. This finding stands in contrast to a recent imaging study reporting
460 differential changes in the rate of Ca^{2+} events in dSPNs and iSPNs upon acute and chronic DA
461 manipulations (Parker et al., 2018). This inconsistency may stem from technical differences: we
462 monitored striatal activity in head-fixed mice consistently performing one simple movement
463 across conditions, whereas Parker et al imaged freely behaving mice performing multiple
464 undefined movement that may vary in frequency or intensity with DA manipulations. In addition,

our imaging approach clearly distinguishes changes in the frequency and amplitude of Ca^{2+} transients per active neuron from changes in the overall number of active cells associated with a given action, which can more easily be conflated with one-photon endoscopic techniques (Helmchen & Denk 2005; Ziv & Ghosh 2015; Zhou et al., 2018). An additional consideration with subcortical cellular-resolution imaging studies is that cortex is necessarily damaged to gain optical access. This is a particularly important caveat in dorsolateral striatum, which receives strong excitatory inputs from the overlaying somatosensory cortex. It is therefore possible that the changes we report here mainly reflect DA modulation of thalamo-striatal circuits, which are preserved in our imaging preparation.

Taken together, our results expand classic rate-based models of DA modulation by revealing an additional dimension of DA signaling at the level of neuronal populations. We find that the size of movement-related SPN ensembles is not fixed, but rather strongly modulated by DA: elevating DA consistently biases striatal ensembles towards the direct pathway, while decreasing DA does the opposite. Importantly, the population dynamics underlying pathway imbalances vary with DA levels and differ in DA-intact and DA-depleted mice, prompting revisions of our understanding of DA's complex modulatory actions *in vivo*. Short and long-term changes in the number of SPNs that fire bursts of action potentials may constitute an integral way in which striatal circuits control the likelihood that a given motor action is selected (Markowitz et al., 2018), the vigor with which it is produced (Panigrahi et al., 2015; da Silva et al., 2018; Yttri & Dudman 2018) and the learning or updating of action sequences (Graybiel 1998; Yin et al., 2009; Koralek et al., 2012; Sheng et al., 2019; Iino et al., 2020). Future investigations will determine the cellular mechanisms that underlie DA's ability to modulate the size of SPN ensembles, the time course of such changes in response to synaptically-released DA, and the impact of varying ensemble size on the production, learning and refinement of motor actions by the basal ganglia.

ACKNOWLEDGEMENTS

We thank Adam Carter, Un Kang, Michael Long, Adam Mar, Margaret Rice, Dick Tsien and members of the Tritsch laboratory for comments on the manuscript. We thank the GENIE Program and the Janelia Research Campus, specifically V. Jayaraman, R. Kerr, D. Kim, L. Looger, and K. Svoboda for making GCaMP6f available. M.M. is supported by a Marlene and Paolo Fresco Postdoctoral Fellowship. N.X.T. is an Alfred P. Sloan Research Fellow in Neuroscience, and is supported by grants from the Dana, Leon Levy and Whitehall Foundations, as well as from the National Institutes of Health (R00NS087098 and DP2NS105553).

503 **AUTHOR CONTRIBUTIONS**
504
505 M.M., J.R.M. and N.X.T. designed and performed experiments, analyzed and interpreted the
506 data, and wrote the manuscript. J.R.M. wrote all custom code. A.G.B. helped with behavioral
507 training and analysis.
508
509
510 **DECLARATION OF INTERESTS**
511
512 The authors declare no competing interests.
513
514
515 **METHODS**
516
517 **Animals.** All procedures were performed in accordance with protocols approved by the NYU
518 Langone Health Institutional Animal Care and Use Committee. Mice were housed in group before
519 surgery and singly after surgery under a reverse 12-hour light-dark cycle (dark from 10 a.m. to 10
520 p.m.) with *ad libitum* access to food and water. *Drd1a*^{tdTomato} transgenic mice (stock #: 016204)
521 and *ChAT*^{Cre} knock-in mice (stock #: 031661) were purchased from The Jackson Laboratory and
522 bred with C57BL/6J wild type mice (stock #: 000664). Transgenic mice expressing Cre selectively
523 in iSPNs (*Adora2a*^{Cre}*;* KG139) or dSPNs (*Drd1a*^{Cre}; EY217) (Gong et al., 2007) were generously
524 provided by Chip Gerfen (NIH) maintained on a C57BL/6J background. Control experiments in
525 **Supplementary Figure 1** were performed using either offspring of *Adora2a*^{Cre} mice bred to a
526 tdTomato reporter (Ai14; The Jackson Laboratory, Stock #: 007908) or *Adora2a*^{Cre} mice injected
527 in dorsolateral striatum with an adeno-associated virus (AAV) encoding Cre-dependent tdTomato
528 (Addgene; #28306-AAV1). Experiments were carried out using both male and female mice
529 heterozygous for all transgenes at 8–24 weeks of age.
530
531 **Surgery.** Mice were administered dexamethasone (4 mg/kg, intraperitoneal) 1–2 hours prior to
532 surgery. They were then anaesthetized with isoflurane, placed in a stereotaxic apparatus (Kopf
533 Instruments) on a heating blanket (Harvard Apparatus) and administered Ketoprofen (10 mg/kg,
534 subcutaneous). The scalp was shaved and cleaned with ethanol and iodine solutions before
535 exposing the skull. A custom titanium headpost was implanted over lambda using C&B metabond
536 (Parkell) to allow head fixation. To achieve widespread viral expression of GCaMP6f in striatum,
537 100 nl of AAV1-Syn-GCaMP6f-WPRE-SV40 (University of Pennsylvania Vector Core) was injected
538 alone or along with AAV1-FLEX-tdTomato (Addgene, #28306) 1.7 mm below dura at a rate of 100
539 nl/min (KD Scientific) into the right dorsolateral striatum at four locations (anterior/lateral from
540 bregma, in mm): 0.7/1.7; 0.7/2.3; 1.3/1.7 and 1.3/2.3. Injection pipettes were left in place for 5

541 min before removal. A 3 mm craniotomy was then drilled (centered at 1.0 mm anterior and 2.0
542 mm lateral from bregma) and cortical tissue was aspirated until the corpus callosum lying above
543 the striatum was exposed, as described previously (Howe & Dombeck 2016; Bloem et al., 2017).
544 A custom 9 gauge thin-walled stainless-steel cannula (Microgroup; 2.3 mm in height) sealed at
545 one end with a 3 mm glass coverslip (Warner Instruments) using optical glue (Norland #71) was
546 placed above the striatum and cemented to the skull using C&B metabond (**Supplementary Fig**
547 **1A, B**). For fiber photometry imaging, 200 nl of AAV1-Syn-FLEX-GCaMP6f-WPRE-SV40 (University
548 of Pennsylvania Vector Core) or AAV9-hSyn-GRAB$_{DA2h}$ (kindly provided by Dr. Yulong Li) was
549 injected 2.2 mm below dura into the right dorsolateral striatum (anterior/lateral from bregma:
550 1.0/2.0) and a 400-µm optic fiber (Thorlabs, FP400URT) housed in a ceramic ferrule (Thorlabs,
551 CFLC440-10) was implanted 0.2 mm above the injection site using C&B metabond. Mice were
552 allowed to recover in their cage for 2 weeks before head-fixation habituation, treadmill training
553 and imaging.
554
555 **6-OHDA lesions.** For experiments characterizing the effects of SNc neuron loss on striatal activity,
556 a second stereotaxic surgery was performed under isoflurane anesthesia after baseline imaging
557 sessions. Desipramine (25 mg/kg) and pargyline (5 mg/kg) were administered intraperitoneally
558 prior to surgery to increase the selectivity and efficacy of 6-OHDA lesions (Thiele et al., 2012). A
559 small craniotomy was performed above the SNc ipsilateral to the imaged striatum (-3.1 mm
560 posterior from bregma, 1.3 mm lateral) and 3 µg of 6-OHDA (total volume: 200 nl) was injected
561 in SNc (4.2 mm below dura) at a rate ~100 nl/min. Sham-lesioned mice were treated identically
562 except that 6-OHDA was omitted from the injected solution (0.2% ascorbic acid in 0.9% sterile
563 NaCl solution). To evaluate motor impairments, mice were placed in a plus maze consisting of 4
564 identical closed arms (length x width x wall height: 45 cm × 7 cm × 15 cm) at 90° to each other
565 and monitored from above with a near infrared camera (Basler; acA2000-165um) for 10 min. All
566 arms of the maze were closed (i.e. featured 15 cm-tall walls) to avoid anxiety-related behaviors.
567 The number of ipsiversive, contraversive and straight choices upon reaching the center of the
568 maze were automatically quantified in MATLAB (Mathworks) and verified visually. Data were
569 expressed as a turning bias index, defined as the difference between ipsiversive and
570 contraversive turns, divided by the total number of turns.
571
572 **Immunohistochemistry.** Mice were deeply anesthetized with isoflurane and perfused
573 transcardially with 4 % paraformaldehyde in 0.1 M sodium phosphate buffer. Brains were post-
574 fixed for 1–3 days, sectioned coronally (50–100 µm in thickness) using a vibratome (Leica;
575 VT1000S) and processed for immunofluorescence staining for tyrosine hydroxylase (Millipore;
576 AB152, 1:1000) and dopamine transporter (Millipore; MAB369, 1:1000) using standard methods.
577 Brain sections were mounted on superfrost slides and coverslipped with ProLong antifade
578 reagent with DAPI (Molecular Probes). Endogenous tdTomato and GCaMP6 fluorescence were

579 not immuno-enhanced. Whole sections were imaged with an Olympus VS120 slide scanning
580 microscope and high resolution images of regions of interest were subsequently acquired with a
581 Zeiss LSM 800 confocal microscope. TH and DAT immunofluorescence were quantified in ImageJ
582 (NIH) by measuring mean pixel intensity in similarly-sized regions of interest in VTA, SNc, dorsal
583 striatum and ventral striatum in both intact and lesioned hemispheres. After subtracting
584 background signal from adjacent unstained brain regions, fluorescence intensity values in the
585 lesioned hemisphere were expressed as a percentage of values measured on the intact side.
586 Three measurements were obtained from each region of interest along the anterior-posterior
587 axis and averaged together for each mouse.
588
589 **Reagents.** Drugs (all from Tocris, unless specified otherwise) were reconstituted and stored
590 according to the manufacturers' recommendations. 6-hydroxydopamine (6-OHDA; Sigma-
591 Aldrich) was dissolved freshly into sterile 0.9% NaCl and 0.2% ascorbic acid immediately prior to
592 administration to minimize oxidation. Working concentration aliquots of desipramine (25
593 mg/kg), pargyline (Sigma-Aldrich; 5 mg/kg), S(-)raclopride (Sigma-Aldrich; 1 mg/kg), SCH23390
594 (Fisher Scientific; 0.2 mg/kg), nomifensine (10 mg/kg), (-)quinpirole (0.3-6 mg/kg), SKF81297 (0.3-
595 6 mg/kg) and L-DOPA (10 mg/kg) were prepared daily in sterile physiological saline and
596 administered intraperitoneally at minimum 10 min prior to experimentation. L-DOPA was co-
597 administered along with the peripheral DOPA decarboxylase inhibitor benserazide hydrochloride
598 (Sigma-Aldrich, 12 mg/kg).
599
600 **Two-Photon Imaging.** Imaging was performed through a 20X long working-distance air objective
601 (Edmund Optics; #58373) on a galvo-resonant scanning microscope (Thorlabs; Bergamo-II)
602 equipped with GaAsP photomultiplier tubes and under the control of ScanImage 5 software
603 (Vidrio Technologies). GCaMP6f and tdTomato were excited a using a pulsed dispersion-
604 compensated Ti:Sapphire laser (Coherent; Chameleon Vision II) tuned to 940 nm (40–80 mW at
605 the sample). Mice were head-fixed above a freely rotating circular treadmill consisting of a 6"
606 plastic saucer (Ware Manufacturing) mounted on a rotary encoder (US Digital, Serial #: MA3-A10-
607 125-B). Motorized, fixed-distance and velocity trials were conducted by connecting a integrated
608 servo motor (Teknic Clearpath: CPM-MCVC-2310S-RQN) to the treadmill to impose 10 s-long
609 fixed-speed (10 cm/s) running bouts every 20 s. Water-rewards (~0.1 ml) were delivered through
610 a spout controlled by an inaudible solenoid (The Lee Company, LHQA0531220H) at 60 s intervals
611 between motorized running bouts. Mouse posture was simultaneously monitored using a near
612 infrared camera (Basler; acA2000-165um), with each video frame triggered by the two-photon
613 imaging frame clock. The latter was recorded in Wavesurfer (https://www.janelia.org/open-
614 science/wavesurfer) to synchronize imaging and behavioral data. Striatal fields of view (500 x 500
615 µm; 1–3 per mouse) near the center of the imaging window were selected based on the
616 expression of GCaMP6f and tdTomato, and were continuously imaged with a resolution of 512 x

617 512 pixels at 30 Hz frame rate for a minimum of 20 min each. Bleaching of GCaMP6f was
618 negligible. The same fields of view were imaged multiple times on non-consecutive days using
619 alignment based on blood vessels and a reference image.
620
621 **Fiber photometry.** Excitation light (Thorlabs; M470F3) was passed through a fluorescence mini-
622 cube (Doric, FMC5-E1-460/490) and 400-µm fiber optic patch cord connected to the mouse via a
623 zirconia sleeve. Emission was collected through the same patch cord and mini-cube to a
624 femtowatt photoreceiver (Newport, 2151). Photometry signals were digitized at 2 kHz using a
625 National Instruments acquisition board (USB-6343), recorded with Wavesurfer, and low-pass
626 filtered and down-sampled to 30Hz in MATLAB (Mathworks).
627
628 **Image Processing.** Time series of two-photon images were concatenated and motion corrected,
629 and Ca^{2+} fluorescence traces were extracted from individual neurons with minimal neuropil
630 contamination using a custom MATLAB (Mathworks) pipeline described in detail in Driscoll et al.
631 (2017) and kindly made available by Chris Harvey (Harvard Medical School;
632 https://github.com/HarveyLab/Acquisition2P_class.git). Briefly, putative cell bodies were
633 selected manually in the mean intensity image. Highly correlated and spatially-contiguous
634 fluorescence sources within 30 µm of the selected pixel were then identified automatically based
635 on the correlation structure of the pixel time series to delineate the spatial footprint of active
636 neuronal processes. Fluorescence time series were computed by averaging across all pixels
637 within that footprint and were manually classified into cell bodies, processes (not analyzed), and
638 background (neuropil). This approach is advantageous over manually defined regions of interest
639 as it segregates dendritic processes that overlap with somata if they exhibit distinct fluorescence
640 time series. Each putative cell was paired with a neighboring background source, which was
641 subtracted from the cell body's fluorescence time series. Segmentation and neuropil subtraction
642 were manually verified for each cell and adjusted when necessary using a graphical user interface
643 to obtain clean neuropil-subtracted fluorescence traces without apparent negative-going
644 transients. GCamp6f-labelled cell bodies were manually labeled as dSPNs or iSPNs based on
645 tdTomato fluorescence in the mean intensity image in *Drd1a*^{tdTomato} and *Adora2a*^{tdTomato} mice,
646 respectively, and tdTomato-negative cells were either labeled as putative iSPNs (in in
647 *Drd1a*^{tdTomato} mice), putative dSPNs (*Adora2a*^{tdTomato} mice), or putative interneurons based on cell
648 morphology, baseline Ca^{2+} fluorescence intensity and Ca^{2+} transient kinetics (**Figure 1** and
649 **Supplementary Figure 1**) by an experimenter blind to experimental conditions.
650
651 **Image and behavior analyses.** Quantification of imaging and behavioral data was carried out in
652 MATLAB using custom-code available online (https://github.com/TritschLab). Ca^{2+} transients
653 were detected using the built-in MATLAB findpeaks() function on each cell's neuropil-subtracted
654 fluorescence trace smoothed with a 150 ms window if they exhibited a minimum peak height

655 and minimum peak prominence of 5 standard deviations greater than baseline, and a minimum
656 width of 140 ms at half peak prominence. These criteria are intentionally stringent so as to
657 exclude events not clearly resolved from baseline fluorescence at the cost of underestimating
658 Ca^{2+} transient frequency per SPN. All imaged neurons displaying at minimum one Ca^{2+} transient
659 were deemed active. Individual fields of view were only selected for longitudinal imaging and
660 quantification if at least five active dSPNs and five active iSPNs were observed at baseline in self-
661 initiated and motorized locomotor trials, and if mice traveled at minimum five meters in self-
662 initiated trials to ensure adequate estimation of SPN ensemble size and mean SPN Ca^{2+} transient
663 frequency. For each imaging session and field of view (FOV), we report the percentage of dSPNs
664 and iSPNs that display Ca^{2+} transients (i.e. active ensemble size), the frequency of Ca^{2+} transients
665 recorded per active dSPNs or iSPNs while moving or immobile averaged across each FOV, and the
666 mean amplitude of Ca^{2+} transients recorded in all active dSPNs or iSPNs averaged for each FOV.
667 Active ensemble size is calculated as the percentage of all imaged dSPNs or iSPNs in a given FOV
668 that display Ca^{2+} transients over the course of an imaging session. Activity in dSPNs and iSPNs
669 was compared for each imaging session and FOV by computing a bias index, consisting of the
670 difference in ensemble size, mean Ca^{2+} transient frequency or amplitude between dSPNs and
671 iSPNs, divided by their sum. Treadmill velocity was extracted from positional information
672 provided by the rotary encoder, down-sampled to 30 Hz and aligned to the two-photon imaging
673 frame rate. Immobility is defined as any period of time beginning at least 0.5 s after treadmill
674 velocity decreases below 0.2 cm/s, lasting at minimum 4 s, and ending 0.5 s before treadmill
675 velocity exceeds 0.2 cm/s again and for which no postural movement is detected using the
676 infrared camera. Movement bouts are defined as any period of time when absolute treadmill
677 velocity exceeds 0.4 cm/s for a minimum of 4 s, and is preceded and followed by 4 s of immobility.
678 Movement onsets and offsets are the first and last time points, respectively, at least two standard
679 deviations away from treadmill velocity measured while immobile. To relate Ca^{2+} transient
680 frequency to treadmill velocity, we recorded the instantaneous treadmill velocity at each Ca^{2+}
681 transient onset and divided the total number of Ca^{2+} transients per velocity (binned at 0.4 cm/s)
682 per SPN by the amount of time spent by a mouse at that velocity over the course of an imaging
683 session. To relate the percentage of active SPNs to velocity, we averaged treadmill velocity in 200
684 ms bins, determined the fraction of all imaged dSPNs or iSPNs active within each bin and
685 calculated the mean percentage of active dSPNs and iSPNs at different treadmill speeds (binned
686 to 0.4 cm/s). To align Ca^{2+} transient frequency to movement onset/offset, we calculated the
687 mean number of Ca^{2+} transients imaged per FOV per 200 ms-long bin around all locomotor bout
688 onsets/offsets divided by the total number of active SPNs and bin duration.
689
690 **Statistical analyses.** Data (reported in text and Figures as mean ± s.e.m) were compared in Prism
691 8 (Graphpad) using non-parametric Mann-Whitney U test for independent groups and Wilcoxon
692 signed-rank test for matched samples, and Two-way ANOVAs (mixed-effect model) for all

693 multiple comparison, as indicated in text and figure legends. Significant interactions were
694 followed-up with within-group pairwise t-tests with baseline or prelesion data corrected for
695 multiple comparisons (Bonferroni). P values smaller than 0.05 were considered statistically
696 significant and assigned the following nomenclature in Figures: * $p < 0.05$, ** $p < 0.01$, *** $p <$
697 0.005 and **** $p < 0.001$. Reported n values represent the number of fields of view imaged from
698 N mice.
699
700
701 **REFERENCES**
702

703 Abercrombie ED, Bonatz AE, Zigmond MJ. 1990. Effects of L-dopa on extracellular dopamine in
704 striatum of normal and 6-hydroxydopamine-treated rats. *Brain Res* 525: 36-44
705 Ade KK, Wan Y, Chen M, Gloss B, Calakos N. 2011. An Improved BAC Transgenic Fluorescent
706 Reporter Line for Sensitive and Specific Identification of Striatonigral Medium Spiny
707 Neurons. *Front Syst Neurosci* 5: 32
708 Akaike A, Ohno Y, Sasa M, Takaori S. 1987. Excitatory and inhibitory effects of dopamine on
709 neuronal activity of the caudate nucleus neurons in vitro. *Brain Res* 418: 262-72
710 Barbera G, Liang B, Zhang L, Gerfen CR, Culurciello E, et al. 2016. Spatially Compact Neural
711 Clusters in the Dorsal Striatum Encode Locomotion Relevant Information. *Neuron* 92:
712 202-13
713 Beaulieu JM, Gainetdinov RR. 2011. The physiology, signaling, and pharmacology of dopamine
714 receptors. *Pharmacol Rev* 63: 182-217
715 Berke JD, Okatan M, Skurski J, Eichenbaum HB. 2004. Oscillatory entrainment of striatal
716 neurons in freely moving rats. *Neuron* 43: 883-96
717 Bittner KC, Milstein AD, Grienberger C, Romani S, Magee JC. 2017. Behavioral time scale
718 synaptic plasticity underlies CA1 place fields. *Science* 357: 1033-36
719 Bloem B, Huda R, Sur M, Graybiel AM. 2017. Two-photon imaging in mice shows striosomes and
720 matrix have overlapping but differential reinforcement-related responses. *Elife* 6
721 Calabresi P, Mercuri N, Stanzione P, Stefani A, Bernardi G. 1987. Intracellular studies on the
722 dopamine-induced firing inhibition of neostriatal neurons in vitro: evidence for D1
723 receptor involvement. *Neuroscience* 20: 757-71
724 Calabresi P, Picconi B, Tozzi A, Di Filippo M. 2007. Dopamine-mediated regulation of
725 corticostriatal synaptic plasticity. *Trends Neurosci* 30: 211-9
726 Carter AG, Sabatini BL. 2004. State-dependent calcium signaling in dendritic spines of striatal
727 medium spiny neurons. *Neuron* 44: 483-93
728 Cenci MA. 2014. Presynaptic Mechanisms of l-DOPA-Induced Dyskinesia: The Findings, the
729 Debate, and the Therapeutic Implications. *Front Neurol* 5: 242
730 Chen TW, Wardill TJ, Sun Y, Pulver SR, Renninger SL, et al. 2013. Ultrasensitive fluorescent
731 proteins for imaging neuronal activity. *Nature* 499: 295-300
732 Cohen JY, Haesler S, Vong L, Lowell BB, Uchida N. 2012. Neuron-type-specific signals for reward
733 and punishment in the ventral tegmental area. *Nature* 482: 85-8

734 Cui G, Jun SB, Jin X, Pham MD, Vogel SS, et al. 2013. Concurrent activation of striatal direct and
735 indirect pathways during action initiation. *Nature* 494: 238-42
736 da Silva JA, Tecuapetla F, Paixao V, Costa RM. 2018. Dopamine neuron activity before action
737 initiation gates and invigorates future movements. *Nature* 554: 244-48
738 Day M, Wokosin D, Plotkin JL, Tian X, Surmeier DJ. 2008. Differential excitability and modulation
739 of striatal medium spiny neuron dendrites. *J Neurosci* 28: 11603-14
740 Driscoll LN, Pettit NL, Minderer M, Chettih SN, Harvey CD. 2017. Dynamic Reorganization of
741 Neuronal Activity Patterns in Parietal Cortex. *Cell* 170: 986-99 e16
742 Dudman JT, Krakauer JW. 2016. The basal ganglia: from motor commands to the control of
743 vigor. *Curr Opin Neurobiol* 37: 158-66
744 Ericsson J, Stephenson-Jones M, Perez-Fernandez J, Robertson B, Silberberg G, Grillner S. 2013.
745 Dopamine differentially modulates the excitability of striatal neurons of the direct and
746 indirect pathways in lamprey. *J Neurosci* 33: 8045-54
747 Fieblinger T, Graves SM, Sebel LE, Alcacer C, Plotkin JL, et al. 2014. Cell type-specific plasticity of
748 striatal projection neurons in parkinsonism and L-DOPA-induced dyskinesia. *Nat*
749 *Commun* 5: 5316
750 Flaherty AW, Graybiel AM. 1994. Input-output organization of the sensorimotor striatum in the
751 squirrel monkey. *J Neurosci* 14: 599-610
752 Fobbs WC, Bariselli S, Licholai JA, Miyazaki NL, Matikainen-Ankney BA, et al. 2020. Continuous
753 Representations of Speed by Striatal Medium Spiny Neurons. *J Neurosci* 40: 1679-88
754 Gerfen CR. 2003. D1 dopamine receptor supersensitivity in the dopamine-depleted striatum
755 animal model of Parkinson's disease. *Neuroscientist* 9: 455-62
756 Gerfen CR, Surmeier DJ. 2011. Modulation of striatal projection systems by dopamine. *Annu*
757 *Rev Neurosci* 34: 441-66
758 Gittis AH, Kreitzer AC. 2012. Striatal microcircuitry and movement disorders. *Trends Neurosci*
759 35: 557-64
760 Gong S, Doughty M, Harbaugh CR, Cummins A, Hatten ME, et al. 2007. Targeting Cre
761 recombinase to specific neuron populations with bacterial artificial chromosome
762 constructs. *J Neurosci* 27: 9817-23
763 Grace AA, Bunney BS. 1984. The control of firing pattern in nigral dopamine neurons: single
764 spike firing. *J Neurosci* 4: 2866-76
765 Graybiel AM. 1998. The basal ganglia and chunking of action repertoires. *Neurobiol Learn Mem*
766 70: 119-36
767 Graybiel AM. 2005. The basal ganglia: learning new tricks and loving it. *Curr Opin Neurobiol* 15:
768 638-44
769 Guo Q, Wang D, He X, Feng Q, Lin R, et al. 2015. Whole-brain mapping of inputs to projection
770 neurons and cholinergic interneurons in the dorsal striatum. *PLoS One* 10: e0123381
771 Hamid AA, Pettibone JR, Mabrouk OS, Hetrick VL, Schmidt R, et al. 2016. Mesolimbic dopamine
772 signals the value of work. *Nat Neurosci* 19: 117-26
773 Helmchen F, Denk W. 2005. Deep tissue two-photon microscopy. *Nat Methods* 2: 932-40
774 Hernandez-Lopez S, Bargas J, Surmeier DJ, Reyes A, Galarraga E. 1997. D1 receptor activation
775 enhances evoked discharge in neostriatal medium spiny neurons by modulating an L-
776 type Ca2+ conductance. *J Neurosci* 17: 3334-42

777 Hernandez-Lopez S, Tkatch T, Perez-Garci E, Galarraga E, Bargas J, et al. 2000. D2 dopamine
778 receptors in striatal medium spiny neurons reduce L-type Ca2+ currents and excitability
779 via a novel PLC[beta]1-IP3-calcineurin-signaling cascade. *J Neurosci* 20: 8987-95
780 Howe M, Ridouh I, Allegra Mascaro AL, Larios A, Azcorra M, Dombeck DA. 2019. Coordination of
781 rapid cholinergic and dopaminergic signaling in striatum during spontaneous movement.
782 *Elife* 8
783 Howe MW, Dombeck DA. 2016. Rapid signalling in distinct dopaminergic axons during
784 locomotion and reward. *Nature* 535: 505-10
785 Iino Y, Sawada T, Yamaguchi K, Tajiri M, Ishii S, et al. 2020. Dopamine D2 receptors in
786 discrimination learning and spine enlargement. *Nature* 579: 555-60
787 Jedrzejewska-Szmek J, Damodaran S, Dorman DB, Blackwell KT. 2017. Calcium dynamics predict
788 direction of synaptic plasticity in striatal spiny projection neurons. *Eur J Neurosci* 45:
789 1044-56
790 Kerr JN, Plenz D. 2002. Dendritic calcium encodes striatal neuron output during up-states. *J*
791 *Neurosci* 22: 1499-512
792 Ketzef M, Spigolon G, Johansson Y, Bonito-Oliva A, Fisone G, Silberberg G. 2017. Dopamine
793 Depletion Impairs Bilateral Sensory Processing in the Striatum in a Pathway-Dependent
794 Manner. *Neuron* 94: 855-65 e5
795 Klaus A, Alves da Silva J, Costa RM. 2019. What, If, and When to Move: Basal Ganglia Circuits
796 and Self-Paced Action Initiation. *Annu Rev Neurosci* 42: 459-83
797 Klaus A, Martins GJ, Paixao VB, Zhou P, Paninski L, Costa RM. 2017. The Spatiotemporal
798 Organization of the Striatum Encodes Action Space. *Neuron* 96: 949
799 Koralek AC, Jin X, Long JD, 2nd, Costa RM, Carmena JM. 2012. Corticostriatal plasticity is
800 necessary for learning intentional neuroprosthetic skills. *Nature* 483: 331-5
801 Kravitz AV, Freeze BS, Parker PR, Kay K, Thwin MT, et al. 2010. Regulation of parkinsonian
802 motor behaviours by optogenetic control of basal ganglia circuitry. *Nature* 466: 622-6
803 Kress GJ, Yamawaki N, Wokosin DL, Wickersham IR, Shepherd GM, Surmeier DJ. 2013.
804 Convergent cortical innervation of striatal projection neurons. *Nat Neurosci* 16: 665-7
805 Lahiri AK, Bevan MD. 2020. Dopaminergic Transmission Rapidly and Persistently Enhances
806 Excitability of D1 Receptor-Expressing Striatal Projection Neurons. *Neuron* 106: 277-90
807 e6
808 Lee SJ, Lodder B, Chen Y, Patriarchi T, Tian L, Sabatini BL. 2020. Cell-type-specific asynchronous
809 modulation of PKA by dopamine in learning. *Nature*
810 Lemos JC, Friend DM, Kaplan AR, Shin JH, Rubinstein M, et al. 2016. Enhanced GABA
811 Transmission Drives Bradykinesia Following Loss of Dopamine D2 Receptor Signaling.
812 *Neuron* 90: 824-38
813 Lerner TN, Kreitzer AC. 2011. Neuromodulatory control of striatal plasticity and behavior. *Curr*
814 *Opin Neurobiol* 21: 322-7
815 Mallet N, Ballion B, Le Moine C, Gonon F. 2006. Cortical inputs and GABA interneurons
816 imbalance projection neurons in the striatum of parkinsonian rats. *J Neurosci* 26: 3875-
817 84
818 Mandelbaum G, Taranda J, Haynes TM, Hochbaum DR, Huang KW, et al. 2019. Distinct Cortical-
819 Thalamic-Striatal Circuits through the Parafascicular Nucleus. *Neuron* 102: 636-52 e7

820 Marcott PF, Mamaligas AA, Ford CP. 2014. Phasic dopamine release drives rapid activation of
821 striatal D2-receptors. *Neuron* 84: 164-76
822 Markowitz JE, Gillis WF, Beron CC, Neufeld SQ, Robertson K, et al. 2018. The Striatum Organizes
823 3D Behavior via Moment-to-Moment Action Selection. *Cell* 174: 44-58 e17
824 Meng C, Zhou J, Papaneri A, Peddada T, Xu K, Cui G. 2018. Spectrally Resolved Fiber Photometry
825 for Multi-component Analysis of Brain Circuits. *Neuron* 98: 707-17 e4
826 Nanou E, Catterall WA. 2018. Calcium Channels, Synaptic Plasticity, and Neuropsychiatric
827 Disease. *Neuron* 98: 466-81
828 Nelson AB, Kreitzer AC. 2014. Reassessing models of basal ganglia function and dysfunction.
829 *Annu Rev Neurosci* 37: 117-35
830 Owen SF, Berke JD, Kreitzer AC. 2018. Fast-Spiking Interneurons Supply Feedforward Control of
831 Bursting, Calcium, and Plasticity for Efficient Learning. *Cell* 172: 683-95 e15
832 Panigrahi B, Martin KA, Li Y, Graves AR, Vollmer A, et al. 2015. Dopamine Is Required for the
833 Neural Representation and Control of Movement Vigor. *Cell* 162: 1418-30
834 Parker JG, Marshall JD, Ahanonu B, Wu YW, Kim TH, et al. 2018. Diametric neural ensemble
835 dynamics in parkinsonian and dyskinetic states. *Nature* 557: 177-82
836 Parker PR, Lalive AL, Kreitzer AC. 2016. Pathway-Specific Remodeling of Thalamostriatal
837 Synapses in Parkinsonian Mice. *Neuron* this issue
838 Pawlak V, Kerr JN. 2008. Dopamine receptor activation is required for corticostriatal spike-
839 timing-dependent plasticity. *J Neurosci* 28: 2435-46
840 Picconi B, Hernandez LF, Obeso JA, Calabresi P. 2018. Motor complications in Parkinson's
841 disease: Striatal molecular and electrophysiological mechanisms of dyskinesias. *Mov*
842 *Disord* 33: 867-76
843 Planert H, Berger TK, Silberberg G. 2013. Membrane properties of striatal direct and indirect
844 pathway neurons in mouse and rat slices and their modulation by dopamine. *PLoS One*
845 8: e57054
846 Reig R, Silberberg G. 2014. Multisensory integration in the mouse striatum. *Neuron* 83: 1200-12
847 Ryan MB, Bair-Marshall C, Nelson AB. 2018. Aberrant Striatal Activity in Parkinsonism and
848 Levodopa-Induced Dyskinesia. *Cell Rep* 23: 3438-46 e5
849 Schiffmann SN, Lledo PM, Vincent JD. 1995. Dopamine D1 receptor modulates the voltage-
850 gated sodium current in rat striatal neurones through a protein kinase A. *J Physiol* 483 (
851 Pt 1): 95-107
852 Shen W, Flajolet M, Greengard P, Surmeier DJ. 2008. Dichotomous dopaminergic control of
853 striatal synaptic plasticity. *Science* 321: 848-51
854 Sheng MJ, Lu D, Shen ZM, Poo MM. 2019. Emergence of stable striatal D1R and D2R neuronal
855 ensembles with distinct firing sequence during motor learning. *Proc Natl Acad Sci U S A*
856 116: 11038-47
857 Sulzer D, Cragg SJ, Rice ME. 2016. Striatal dopamine neurotransmission: regulation of release
858 and uptake. *Basal Ganglia* 6: 123-48
859 Sun F, Zhou J, Dai B, Qian T, Zeng J, et al. 2020. Next-generation GRAB sensors for monitoring
860 dopaminergic activity in vivo. *Nat Methods* 17: 1156-66
861 Thiele SL, Warre R, Nash JE. 2012. Development of a unilaterally-lesioned 6-OHDA mouse model
862 of Parkinson's disease. *J Vis Exp*

863 Tritsch NX, Sabatini BL. 2012. Dopaminergic modulation of synaptic transmission in cortex and
864 striatum. *Neuron* 76: 33-50
865 Turner RS, Desmurget M. 2010. Basal ganglia contributions to motor control: a vigorous tutor.
866 *Curr Opin Neurobiol* 20: 704-16
867 Vijayraghavan S, Wang M, Birnbaum SG, Williams GV, Arnsten AF. 2007. Inverted-U dopamine
868 D1 receptor actions on prefrontal neurons engaged in working memory. *Nat Neurosci*
869 10: 376-84
870 Wall NR, De La Parra M, Callaway EM, Kreitzer AC. 2013. Differential innervation of direct- and
871 indirect-pathway striatal projection neurons. *Neuron* 79: 347-60
872 Yin HH, Mulcare SP, Hilario MR, Clouse E, Holloway T, et al. 2009. Dynamic reorganization of
873 striatal circuits during the acquisition and consolidation of a skill. *Nat Neurosci* 12: 333-
874 41
875 Yttri EA, Dudman JT. 2016. Opponent and bidirectional control of movement velocity in the
876 basal ganglia. *Nature* 533: 402-6
877 Yttri EA, Dudman JT. 2018. A Proposed Circuit Computation in Basal Ganglia: History-Dependent
878 Gain. *Mov Disord* 33: 704-16
879 Zhai S, Shen W, Graves SM, Surmeier DJ. 2019. Dopaminergic modulation of striatal function
880 and Parkinson's disease. *J Neural Transm (Vienna)* 126: 411-22
881 Zhou P, Resendez SL, Rodriguez-Romaguera J, Jimenez JC, Neufeld SQ, et al. 2018. Efficient and
882 accurate extraction of in vivo calcium signals from microendoscopic video data. *Elife* 7
883 Zhuang X, Mazzoni P, Kang UJ. 2013. The role of neuroplasticity in dopaminergic therapy for
884 Parkinson disease. *Nat Rev Neurol* 9: 248-56
885 Ziv Y, Ghosh KK. 2015. Miniature microscopes for large-scale imaging of neuronal activity in
886 freely behaving rodents. *Curr Opin Neurobiol* 32: 141-7
887

SUPPLEMENTARY FIGURES AND LEGENDS

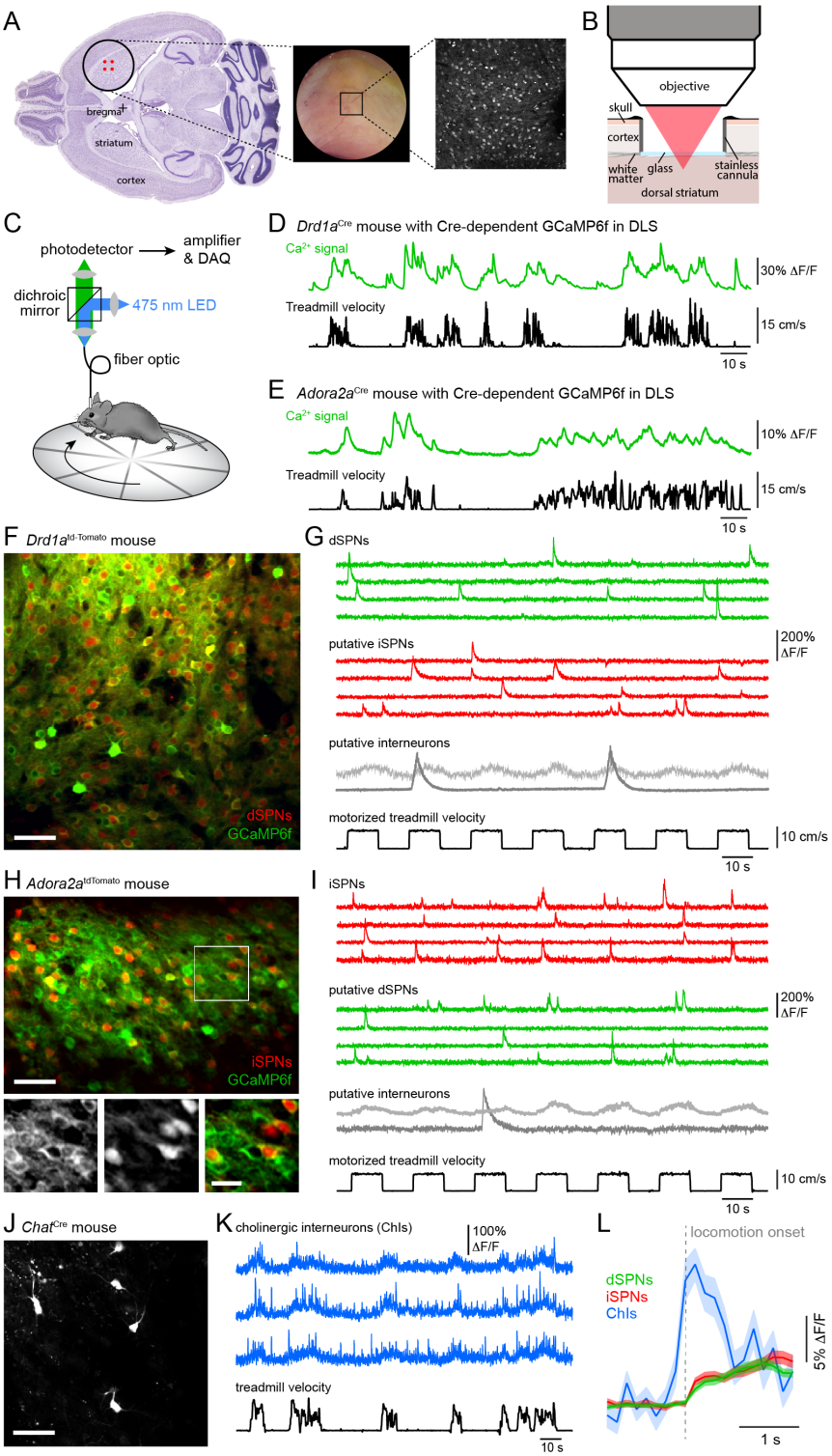

Supplementary Figure 1. Distinguishing Ca^{2+} signals in dSPNs, iSPNs and interneurons *in vivo*.

893 **A.** *Left:* diagram of two-photon imaging window placement relative to bregma on horizontal brain section, with
894 location of viral injections indicated in red. *Middle:* picture of representative imaging window two weeks post-
895 implantation. *Right*: example two-photon image of tdTomato-positive dSPNs in a 500 x 500 μm FOV.
896 **B.** Schematic of two-photon imaging preparation in sagittal plane. To gain optical access to dorsal striatum, the
897 overlaying cortex is removed and replaced with a stainless steel canula fitted with a glass coverslip.
898 **C.** Fiber photometry experimental setup.
899 **D.** Fiber-photometry recording (*top*) and treadmill velocity (*bottom*) recorded from a *Drd1a*^{Cre} mouse virally
900 expressing Cre-dependent GCaMP6f in dorsolateral striatum. Population Ca^{2+} fluorescence is elevated
901 throughout bouts of forward locomotion.
902 **E.** Same as **B** for an *Adora2a*^{Cre} mouse expressing GCaMP6f in iSPNs.
903 **F.** *In vivo* two-photon maximum projection image of dorsolateral striatum in a *Drd1a*$^{td\text{-}Tomato}$ mouse expressing
904 tdTomato in dSPNs and Cre-independent GCaMP6f (AAV1-Syn-GCaMP6f) in all neurons. Scale bar: 50 μm.
905 **G.** Example Ca^{2+} fluorescence traces from four active dSPNs (green), four putative dSPNs (red) and two putative
906 interneurons in FOV shown in **D**. *Bottom*: treadmill velocity during motorized trials (black).
907 **H.** Same as **D** for an *Adora2a*^{Cre} mouse virally expressing a red Cre-dependent reporter in iSPNs (AAV1-FLEX-
908 tdTomato) and Cre-independent GCaMP6f (AAV1-Syn-GCaMP6f) in all neurons. Scale bar: 60 μm. *Inset*: Detail
909 of boxed area in green (*left*), red (*middle*) and merged (*right*) channels. Scale bar: 20 μm.
910 **I.** Example Ca^{2+} fluorescence traces from four active iSPNs (red), four putative dSPNs (green) and two putative
911 interneurons in FOV shown in **F**. *Bottom*: treadmill velocity during motorized trials (black).
912 **J.** Same as **D** for a *Chat*^{Cre} mouse virally expressing Cre-dependent GCAMP6f (AAV1-FLEX-Syn-GCaMP6f) in
913 cholinergic interneurons. Scale bar: 80 μm.
914 **K.** Ca^{2+} fluorescence traces from three active cholinergic interneurons (blue) as mice self-initiate locomotor bouts
915 on a free-spinning treadmill (black).
916 **L.** Mean (± s.e.m in shaded area) Ca^{2+} signal across all active dSPNs (green), iSPNs (red) and cholinergic
917 interneurons (blue) aligned to locomotion onset.
918

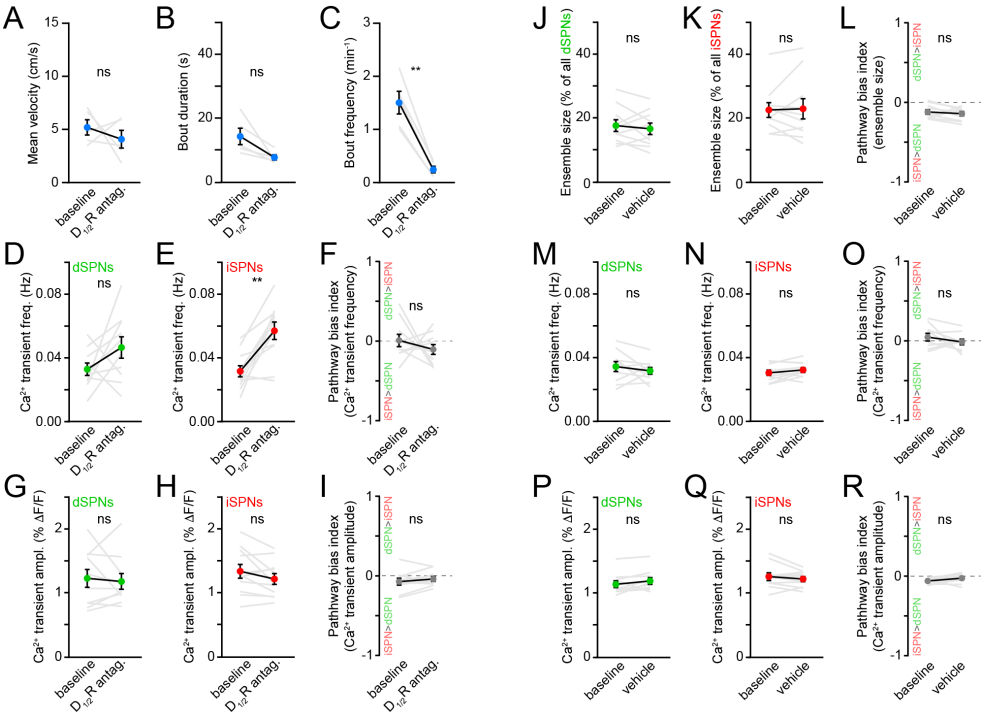

Supplementary Figure 2. Behavior and SPN Ca^{2+} transient properties with DA receptor antagonists.

A. Mean self-initiated treadmill velocity before and after systemic administration of $D_{1/2}R$ antagonists (N = 5 mice, p = 0.62 vs. baseline, Wilcoxon signed-rank).
B. Same as **A** for locomotor bout duration (p = 0.06, Wilcoxon signed-rank).
C. Same as **A** for bout frequency (p = 0.001, Wilcoxon signed-rank).
D. Mean Ca^{2+} transient frequency per dSPN active during locomotion before and after systemic administration of $D_{1/2}R$ antagonists (p = 0.19, Wilcoxon signed-rank).
E. Same as **D** for iSPNs (p = 0.003, Wilcoxon signed-rank).
F. Same as **D** for bias in frequency between pathways (p = 0.49, Wilcoxon signed-rank).
G. Mean Ca^{2+} transient amplitude per dSPN active during locomotion before and after systemic administration of $D_{1/2}R$ antagonists (p = 0.85, Wilcoxon signed-rank).
H. Same as **G** for iSPNs (p = 0.21, Wilcoxon signed-rank).
I. Same as **G** for bias in amplitude between pathways (p = 0.21, Wilcoxon signed-rank).
J. Percentage of all imaged dSPNs showing Ca^{2+} transients during locomotion before and after systemic administration of vehicle (n = 10 FOVs in 5 mice, p = 0.58 vs. baseline, Wilcoxon signed-rank). Mean ± s.e.m are overlaid.
K. Same as **J** for iSPNs (p = 0.97, Wilcoxon signed-rank).
L. Bias in the size of active dSPN and iSPN ensembles before and after vehicle treatment (p = 0.56, Wilcoxon signed-rank).
M. Mean Ca^{2+} transient frequency per dSPN active during locomotion before and after systemic administration of vehicle (p = 0.37, Wilcoxon signed-rank).
N. Same as **M** for iSPNs (p = 0.19, Wilcoxon signed-rank).
O. Same as **M** for bias in frequency between pathways (p = 0.56, Wilcoxon signed-rank).
P. Mean Ca^{2+} transient amplitude per dSPN active during locomotion before and after systemic administration of vehicle (p = 0.06, Wilcoxon signed-rank).
Q. Same as **P** for iSPNs (p = 0.37, Wilcoxon signed-rank).
R. Same as **P** for bias in amplitude between pathways (p = 0.10, Wilcoxon signed-rank).

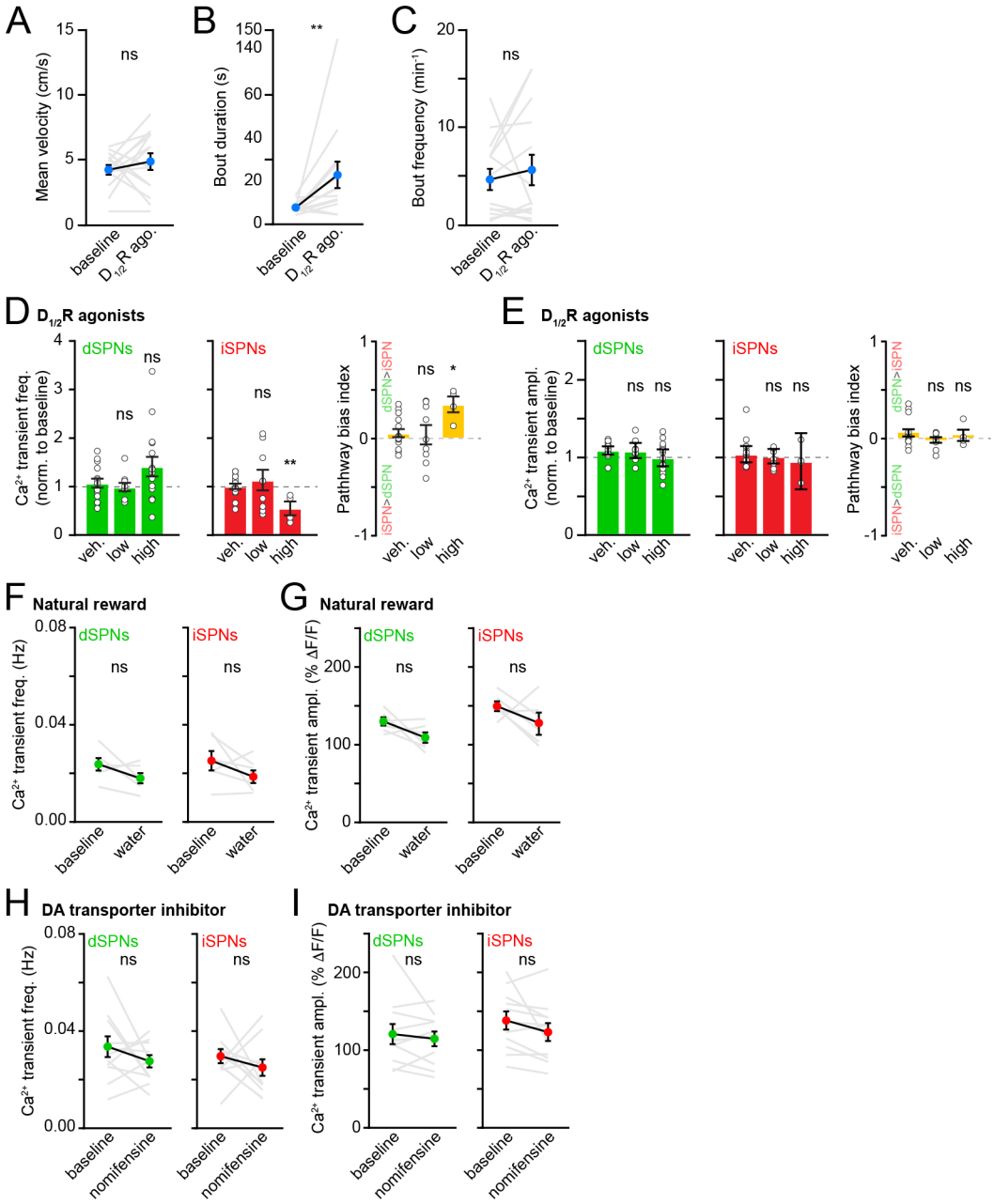

Supplementary Figure 3. Behavior and SPN Ca^{2+} transient properties following increased DA receptor signaling.

A. Mean self-initiated treadmill velocity before and after systemic administration of $D_{1/2}R$ agonists (N = 14 mice, p = 0.38 vs. baseline, Wilcoxon signed-rank).

B. Same as **A** for locomotor bout duration (p = 0.002, Wilcoxon signed-rank).

C. Same as **A** for bout frequency (p = 0.40, Wilcoxon signed-rank).

D. Mean Ca^{2+} transient frequency per dSPN (*left*) or iSPN (*middle*) active during locomotion after systemic administration of vehicle (n = 15 FOVs in 10 mice) and $D_{1/2}R$ agonists at different concentrations (low: 0.3-1 mg/kg; high: 3-6 mg/kg) normalized to pre-drug baseline (dSPNs: low p = 0.58; high p = 0.27; iSPNs: low p > 0.99; high p = 0.006, all vs. vehicle, Mann-Whitney). *Right*: Bias in Ca^{2+} transient frequency between pathways (low: p = 0.81; high: p = 0.01, all vs. vehicle, Mann-Whitney).

E. Same as **D** for Ca^{2+} transient amplitude (dSPNs: low p = 0.83, high p = 0.18; iSPNs: low p = 0.89, high p = 0.58; bias: low p = 0.38, high p = 0.66; all vs. vehicle, Mann-Whitney).

961 **F.** Mean Ca^{2+} transient frequency per dSPNs (*left*, green) and iSPNs (*right*, red) active during locomotion in a
962 baseline (non-rewarded) imaging session vs. a session in which were delivered water rewards between
963 locomotor bouts (dSPNs: $p = 0.16$; iSPNs: $p = 0.22$; all vs. baseline, Wilcoxon signed-rank).
964 **G.** Same as **F** for Ca^{2+} transient amplitude (dSPN: $p = 0.16$; iSPN: $p = 0.22$; all vs. baseline, Wilcoxon signed-rank).
965 **H.** Same as **F** for before (baseline) and after pharmacological elevation of DA in striatum with the DA transporter
966 inhibitor nomifensine (dSPNs: $p = 0.41$; iSPNs: $p = 0.58$; all vs. baseline, Wilcoxon signed-rank).
967 **I.** Same as **H** for Ca^{2+} transient amplitude (dSPNs: $p = 0.64$; iSPNs: $p = 0.08$; all vs. baseline, Wilcoxon signed-rank).
968

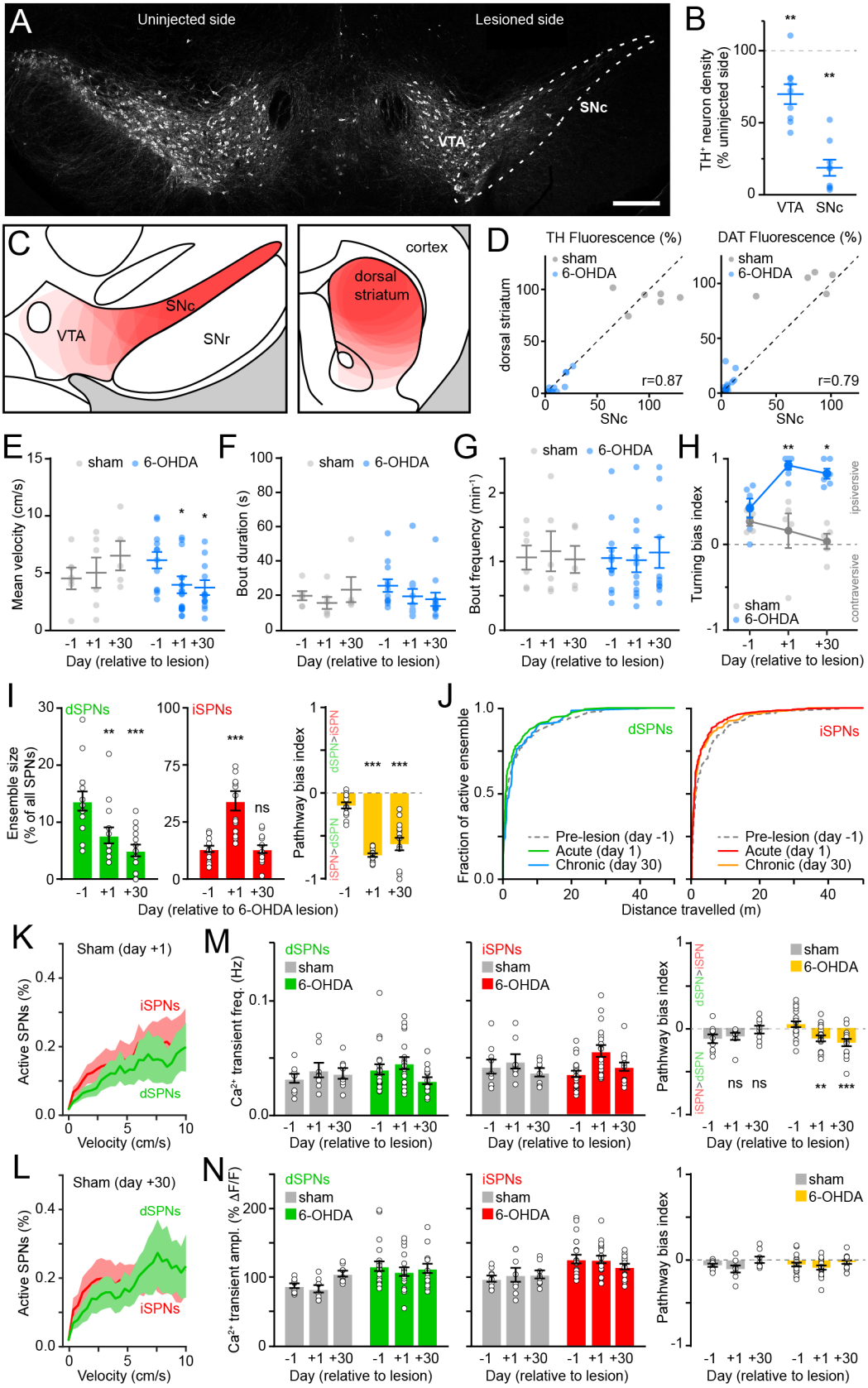

Supplementary Figure 4. Characterization of striatal activity in sham and 6-OHDA treated mice.

971 **A.** Confocal image of a coronal midbrain section immunostained for tyrosine hydroxylase (TH) 24 h after unilateral
972 injection of 6-OHDA in SNc (dashed outline). Scale bar: 300 μm.
973 **B.** Number of TH-positive neurons identified in SNc and VTA on injection side relative to contralateral side 24 h
974 after intracranial injection of 6-OHDA in SNc (n = 9 sections from 3 mice; VTA: p = 0.008; SNc: p = 0.004; Wilcoxon
975 signed rank).
976 **C.** Schematic coronal sections of ventral midbrain (*left*; -3.1 mm from bregma) and forebrain (*right*; +1 mm from
977 bregma) illustrating 6-OHDA-mediated loss of DA neuron cell bodies in SNc/VTA and DA axons in striatum,
978 respectively. The extent of the lesion is indicated in light red for each mouse and the results of 12 mice used
979 for two-photon imaging are overlaid. SNr: substantia nigra pars reticulata.
980 **D.** Comparison of TH (*left*) and DAT (*right*) fluorescence (reported as % from control, uninjected hemisphere) in
981 dorsal striatum vs. SNc in sham (gray; N = 6) and 6-OHDA lesioned (blue; N = 12) mice used for two-photon
982 imaging. Dashed black line: unity. *r*: Spearman correlation coefficient.
983 **E.** Mean self-initiated treadmill velocity before (day -1), 1 day after and 30 days after unilateral injection of vehicle
984 (N = 6, gray) or 6-OHDA (N = 12, blue) in SNc (Two-way ANOVA lesion x time: $F_{2,30} = 5.56$, p = 0.009; sham: day 1
985 p > 0.99; day 30 p = 0.14; 6-OHDA: day 1 p = 0.035; day 30 p = 0.033; all vs. day -1, within-group post-hoc
986 Bonferroni).
987 **F.** Same as **C** for locomotor bout duration (Two-way ANOVA lesion x time: $F_{2,30} = 0.99$, p = 0.38).
988 **G.** Same as **C** for bout frequency (Two-way ANOVA lesion x time: $F_{2,30} = 0.15$, p = 0.86).
989 **H.** Turning bias measured in a closed-arm plus maze in a subset of vehicle (N = 5, gray) and 6-OHDA injected mice
990 (N = 6, blue) 1 day before, 1 day after and 30 days after intracranial surgery. Values approaching 1 and -1 reflect
991 strong turning bias toward (ipsiversive) or away from (contraversive) the lesioned hemisphere, respectively
992 (Two-way ANOVA lesion x time: $F_{2,27} = 6.0$, p = 0.007**;** sham: day 1 p = 0.98; day 30 p = 0.28; 6-OHDA: day 1 p =
993 0.003; day 30 p = 0.015; all vs. day -1, within-group post-hoc Bonferroni).
994 **I.** Size of dSPN (*left*) and iSPN (*middle*) ensembles recruited during fixed-velocity locomotion on a motorized
995 treadmill and their relative bias (*right*) immediately before (day -1), 1 day after or 30 days after unilateral 6-
996 OHDA injection in SNc (dSPNs: day 1 p = 0.003; day 30 p = 3.7×10^{-4}; iSPNs: day 1 p = 1.2×10^{-4}, day 30 p = 0.88;
997 pathway bias: day 1 p = 1.2×10^{-4}, day 30 p = 1.2×10^{-4}; all vs. day -1, Wilcoxon signed-rank).
998 **J.** Cumulative distribution of active dSPNs (*left*) and iSPNs (*right*) recruited as a function of distance travelled 1 day
999 before (pre-lesion), 1 day after (acute) or 30 days after (chronic) unilateral 6-OHDA injection in SNc.
1000 **K.** Percentage of imaged dSPNs (green) and iSPNs (red) displaying Ca^{2+} transients per 200 ms-time bins vs. mean
1001 treadmill velocity during self-initiated forward locomotion on day 1 after vehicle injection in SNc (sham). Shaded
1002 area is s.e.m.
1003 **L.** Same as **I** for day 30.
1004 **M.** Mean Ca^{2+} transient frequency per dSPN (*left*) and iSPNs (*middle*) active during self-initiated movement 1 day
1005 before, 1 day after, or 30 days after sham (n = 9 FOVs in 6 mice) or 6-OHDA lesions (n = 21 FOVs from 12 mice;
1006 Two-way ANOVA lesion x time: dSPN, $F_{2,45} = 1.05$, p = 0.36; iSPN, $F_{2,45} = 1.64$, p = 0.21). *Right*: Ca^{2+} transient
1007 frequency bias between pathways (Two-way ANOVA lesion x time: $F_{2,45} = 7.98$, p = 0.001; sham: day 1 p > 0.9;
1008 day 30 p = 0.23; 6-OHDA: day 1 p = 0.008; day 30 5.0×10^{-4}; all vs. day -1; within-group post-hoc Bonferroni).
1009 **N.** Same as **K** for Ca^{2+} transient amplitude (Two-way ANOVA lesion x time: dSPN: $F_{2,45} = 1.31$, p = 0.3; iSPN: $F_{2,45}$ =
1010 1.50, p = 0.2).
1011

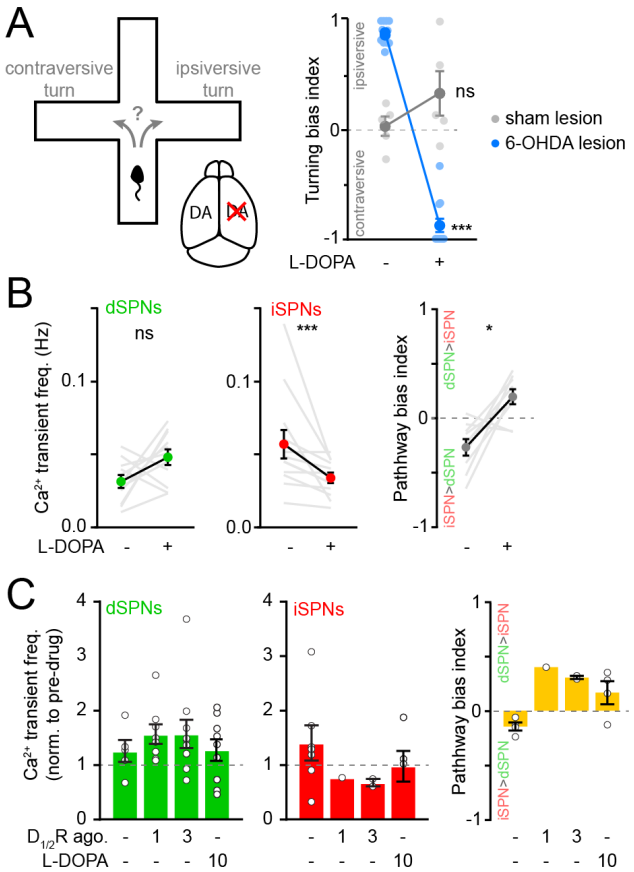

Supplementary Figure 5. Chronic DA depletion SPN ensembles affects differently striatal activity

A. *Left*, diagram of closed-arm plus maze and unilateral DA depletion. *Right*, Turning bias measured before and after L-DOPA treatment in DA-intact (N = 5, gray) and chronically DA-depleted mice (N = 12, blue; Two-way ANOVA lesion x levodopa: $F_{1,30} = 141.3$, $p = 7.1 \times 10^{-13}$; DA-intact: $p = 0.1$; DA-depleted: $p < 1 \times 10^{-15}$; all vs. baseline, post-hoc Bonferroni).

B. Mean Ca^{2+} transient frequency per dSPN (*left*) and iSPN (*middle*) active in chronically-lesioned mice before and after elevating striatal DA with L-DOPA (dSPN: $p = 0.10$; iSPN: $p = 4.9 \times 10^{-4}$; all vs. baseline, Wilcoxon signed rank). *Right*: frequency bias index ($p = 0.02$ vs. baseline, Wilcoxon signed rank). Mean ± SEM are overlaid for each group.

C. Mean Ca^{2+} transient frequency per dSPN (*left*) and iSPN (*middle*) active in chronically-lesioned mice after systemic administration of $D_{1/2}R$ agonists (dSPNs: 1 mg/kg $p = 0.43$; 3 mg/kg: $p = 0.44$; iSPNs: 3 mg/kg $p = 0.22$; all vs. vehicle; Mann-Whitney) and L-DOPA (dSPNs: $p = 0.80$; iSPNs: $p = 0.34$; all vs. vehicle; Mann-Whitney) normalized to pre-drug baseline. *Right*: Bias in Ca^{2+} transient frequency between pathways (3 mg/kg: $p = 0.13$; L-DOPA: $p = 0.08$; all vs. vehicle, Mann-Whitney).

Supplementary Video.

Two-photon time lapse series (30 Hz frame rate) of Gcamp6f fluorescence in dorsolateral striatum as mice engage in bouts of self-paced forward locomotion. Replay speed: 1x.